Department of Physics and Astronomy
Heidelberg University

Bachelor Thesis in Physics
submitted by

Marius Baumann

born in Kirchheim u. Teck (Germany)

03.09.2002

Integrated photonics on Indium phosphide for optical Neuromorphic Computing

This Bachelor Thesis has been carried out by Marius Baumann at the
Kirchhoff-Institute of physics in Heidelberg
under the supervision of
Prof. Dr. Wolfram Pernice and Apl. Prof. Dr. Ulrich Schmidt

Abstract

For optical neuromorphic computing, silicon is widely used as a platform for photonic integrated circuits (PICs). However, since silicon is an indirect bandgap semiconductor, the integration of many active components is difficult. For this purpose, the direct bandgap semiconductor indium phosphide (InP) is an interesting alternative to silicon as a platform. Hence, this thesis focuses on testing InP chips for optical neuromorphic computing. Two InP-based chips with different test structures were used to characterize the on-chip active devices. Therefore, the spectra of the lasers and the manipulation of these spectra by the amplifiers and modulators were analyzed in DC mode. The current-voltage characteristics of the components have been measured, it has been inspected how to optimize the conduction of the on-chip modulators for high-frequency applications by determining the S-parameters, and an attempt has been made to determine the electrical bandwidth of the modulators. Furthermore, an attempt has been tried to implement a neuromorphic application based on the concept of time-wavelength interleaving.

The result was that the laser sources, photodiodes, and modulators performed as expected to be used in further applications. The modulators are best working for high frequency by terminating the device with a parallel resistor and by optimizing the conduction on the circuit board that provides the electric connection to the chip. The on-chip amplifiers do not perform as expected since the signal-to-noise ratio for some of the amplifiers is quite below expectations. Due to that, it was not possible to obtain electrical bandwidth results. It was also not possible to implement time-wavelength interleaving. Nevertheless, it can be concluded that InP chips definitely have great potential as light sources and detectors for further experiments in the research group, since the lasers, modulators, and detectors worked as expected.

Für optisches neuromorphes Rechnen wird Silizium aufgrund seiner vorteilhaften Eigenschaften häufig als Plattform für photonische integrierte Schaltungen (PICs) verwendet. Da Silizium jedoch ein Halbleiter mit indirekter Bandlücke ist, ist die Integration vieler aktiver Komponenten, insbesondere von Lasern, schwierig. Für diesen Zweck ist der Halbleiter Indiumphosphid (InP) mit direkter Bandlücke eine interessante Alternative zu Silizium als Plattform. Daher konzentriert sich diese Arbeit auf das Austesten von InP-Chips für optisches neuromorphes Rechnen. Zwei InP-Chips mit unterschiedlichen Teststrukturen wurden verwendet, um die aktiven Bauelemente auf dem Chip zu charakterisieren. Dazu wurden die Spektren der Laser und die Manipulation dieser Spektren durch die Verstärker und Modulatoren für Gleichstrom getestet. Die Strom-Spannungs-Kennlinien der Komponenten wurden gemessen, es wurde analysiert, wie die Leitung der On-Chip-Modulatoren für Hochfrequenzanwendungen durch die Bestimmung der S-Parameter optimiert werden kann und es wurde versucht, die elektrische Bandbreite der Modulatoren zu bestimmen. Darüber hinaus wurde versucht, eine neuromorphe Anwendung zu implementieren, die auf dem Konzept der Zeit-Wellenlängen-Verschränkung basiert.

Das Ergebnis war, dass die Laserquellen, Photodioden und Modulatoren wie erwartet funktionierten, um in weiteren Anwendungen benutzt zu werden. Die Modulatoren funktionieren am besten für hohe Frequenzen, indem das Gerät mit einem Parallelwiderstand abgeschlossen wird und die Leitungen auf der Leiterplatte, die die elektrische Verbindung zum Chip herstellt, optimiert werden. Die On-Chip-Verstärker zeigen nicht zuverlässig die erwartete Leistung. Das Verhältnis von Signal zu Rauschen blieb unter den Erwartungen. Infolgedessen war es nicht möglich, Ergebnisse zur elektrischen Bandbreite zu erhalten, weshalb es auch nicht möglich war, Zeit-Wellenlängen-Verschränkung zu implementieren. Nichtsdestotrotz kann aus diesen Ergebnissen geschlossen werden, dass InP-Chips definitiv ein großes Potenzial als Lichtquellen und Detektoren für weitere Experimente in der Arbeitsgruppe, da die Laser, Modulatoren und Detektoren wie erwartet funktioniert haben.

Contents

1 Introduction

In recent years, the limitations of the Von Neumann architecture, the classical computing architecture, have become increasingly apparent due to the growing demand for data and artificial intelligence (AI) applications [1]. The von Neumann architecture separates the data memory from the data processing, but this approach is becoming less effective with an increasing amount of data due to the bottleneck of data exchange between memory and processor. Because of that, so-called hardware accelerators were developed that are optimized to tackle computationally intensive tasks like matrix-vector multiplication. Those computationally intensive tasks are often necessary for machine learning and AI applications. Examples of hardware accelerators are Field-programmable gate arrays (FPGAs), graphics processing units (GPUs), and application-specific integrated circuits (ASICs) [2]. A rather new approach to dealing with the limitations of the Von Neumann architecture is the approach of 'neuromorphic' computing. Neuromorphic means in that context computing in a brain-inspired way in neural networks. But in recent times, this term has been understood more widely to make use of principles of how the brain works [3]. For neuromorphic computing, these brain-inspired principles are highly parallel processing and in-memory computing. An electronic approach for neuromorphic computing are crossbar arrays out of memristive components [4]. Memristive means that the components change their internal resistance state dependent on the history of experienced voltages [5]. Those crossbar arrays can be understood as a physical realization of a matrix structure with the states of the memristive components as the matrix elements, so that this structure can do matrix vector multiplications. The calculation is represented by input voltages as the input vector to be multiplied and the output currents as the resulting output vector according to Ohm's law [4]. This approach to matrix vector multiplication promises much more efficiency than the approach of the Von Neumann architecture. The reason for that is that the neuromorphic approach calculates different multiplications simultaneously, so this approach is highly parallelised.

However, not only the classical computing architecture but also electronics itself faces limitations like parasitic capacitances and electromagnetic interference [6]. Optical computing is an interesting approach to deal also with these limitations and enables some advantageous features: It allows a large increase in parallelization due the possibility of utilizing different properties of light for multiplexing. Multiplexing means that different signals are propagating on one shared device. For light, the suitable properties for multiplexing are the polarization, the propagation mode, or the wavelength (Wavelength Division Multiplexing (WDM)) [7]. For WDM it is beneficial that the optical bandwidth is typically large. Furthermore, optical computing can be less energy-intensive since charging and discharging of electronic devices for data movement is unnecessary, contrary to electronics [8]. The described electronic approach to neuromorphic computing can also be done optically, utilizing the above-mentioned advantages. Instead of electrical currents and voltages, the power of the ligth signals represent the input and output vectors, and instead of memristive components for crossbar arrays, the matrix elements correspond to the transmittance of a partly absorbing, partly transmitting material [9].

1.1 Platforms for photonic integrated circuits (PIC)

Similar to electronic computing, optical computing can be done on a microchip in an integrated circuit. On an PIC, there are different active and passive optical components that manipulate or generate the light signals. Those components are connected by on-chip waveguides in which the light propagates [10]. The material from which the chip is made of is called the platform of the PIC. Widely used platforms for PICs are silicon or silicon nitride due to several reasons: The material is cheap, it is compatible with Complementary metal–oxide–semiconductor (CMOS) technology and a large yield is enabled. Also, the footprint of the waveguides can be made very small due to the high index contrast between the core and the substrate of the waveguides [11]. However, due to the indirect band gap of silicon, it is challenging, inefficient, or even not possible to realize active components like detectors, amplifiers, modulators, and especially laser sources. To build those active components, direct band gap semiconductors are much more suitable. Indium phosphide (InP) is such a direct band gap semiconductor that allows the monolithic integration of a variety of active devices on-chip [12]. However, InP comes with disadvantages: It is an expensive material, the index contrast is quite low between the core material and the substrate, and the propagation loss is rather large [11]. In this context, another approach is so-called hybrid integration. Hybrid means that two or more chips are used that are optically connected: One chip on a silicon (or other) platform takes advantage of the passive structures of silicon-based photonics. A second chip on an InP platform contains the light sources, detectors, and other active components for which a direct bandgap semiconductor is more suitable [13].

1.2 Objectives and structure of this thesis

The objective of this thesis is to characterize the active components on InP-chips and assess their suitability for future applications. Therefore, two different InP chips manufactured by the Heinrich-Hertz Institute of the Fraunhofer Institute will be used for the experiments. One chip features 16 lasers, so this chip will be referred to as the "Laserchip". The other chip's main structure is comprised of 16 photo diodes, so it will be referred to as the "Detectorchip". Additionally, both chips contain further structures that will help estimate the properties of the components in both DC and AC operations.

Furthermore, the aim is to assess the potential for optimizing the design of the chips and also the printed circuit boards (PCBs) which can be optimized regarding high frequency. Ultimately, the objective is to use the Detectorchip and Laserchip in subsequent experiments within a hybrid configuration, where they serve as both sources and detectors for other PICs. For this purpose the structure of 16 photo diodes and 16 lasers with different wavelengths could be connected to a crossbar array. So the final goal with these chips would be to have a closed system of three PICs (Laserchip, detectorchip and the chip with the crossbar array) to perform matrix-vector multiplication.

In addition to testing the active structures, the objective is to use one structure on the Laserchip as a hardware accelerator for convolution operations based on time-wavelength interleaving. This method makes use of the distinct dispersion relations of different wavelengths [14].

Structure of this thesis In the second chapter of this thesis, the theory behind the fundamental photonic building blocks, the electronic concepts and the theory behind time-wavelength-interleaving are introduced. The experimental setup is presented in the third chapter. In chapter four, the experiments are described and the obtained data is shown. The fifth chapter is about the conclusions that are made from the experiments. In the appendix, a description of all experimental devices can be found.

2 Theory

2.1 Building blocks of PICs

The central aspect of this bachelor's thesis will be to test the photonic building blocks on the InP-chips with a particular focus on the active components. In a PIC, there can be both active and passive building blocks. Active building blocks are those that have an electrical connection and can be controlled by that. Instead of that, passive building blocks operate solely in an optical manner [15].

2.1.1 Passive building blocks

Waveguides and modes in fiber Waveguides are the basis of integrated photonics since they connect the different components with each other. In waveguides, light is guided using the same principle as for optical fibers which is internal total reflection. Therefore, every waveguide is constructed from a core with a higher refractive index and cladding with a lower refractive index [15]. For the InP-chips, the core material is iron doped InGaAsP (Fe-Q(1.06)), while the cladding to the top and the side is air and the cladding to the bottom is the substrate which is iron doped InP (Fe-InP) [16]. Due to that for InP as a platform, the mode confinement is really good only in the horizontal direction, because the refractive index difference between core and air is high, but the one between core and substrate is much worse comparing to the index difference for other platforms [11]. For a given waveguide, there are discrete modes in which light propagates. The modes can be classified as transverse electric (TE) or transverse magnetic (TM) modes, depending on whether the transverse component of the electric field or the transverse component of the magnetic field disappears [15]. The lasers on the InP-chip emit light in the fundamental TE mode. Since different modes propagate differently in the structure, it is advantageous to only work with a geometry that allows a single fiber mode.

Multi-mode intereferometer (MMI) and multiplexing MMIs are employed to split optical signals from a single waveguide to multiple waveguides, or alternatively, to combine the signal from multiple waveguides into a single signal. The MMIs utilized on the chips are 1x2 MMIs [17]. When combining two signals with an MMI, both signals will experience a loss of 3 dB due to the geometry of the MMI, plus the insertion loss of the device.

Spot size converters (SSCs) To couple light into or out of the chip, we use SSCs. SSCs increase the size of the mode in the waveguide so that it matches the size of the bigger mode in the fibers. This way of coupling is called edge-coupling or facet-coupling. The most common form of facet coupling to a chip is through a single-mode fiber. Since for many applications, multiple inputs and outputs are of interest, multiple fibers have to be coupled to the chip simultaneously. This can be done with a so-called fiber array that matches the pitch of the SSCs [18].

To optimize the coupling efficiency, the polishing angle of the fiber array has to be adjusted. This angle can be calculated using Snell's law [15]. Also, the overlap of the fiber mode and the SSC mode is dependent on the distance between the fiber and the SSC since the light cone becomes increasingly wider and therefore the overlap is smaller for greater distances. So for coupling, it is necessary to get the fiber as close as possible to the SSC.

Active-passive transition For each transition between an active and a passive component, a specific structure is required, which is referred to as a butt-joint. Avoiding these transitions is beneficial since each butt-joint connection exhibits an intrinsic insertion loss [18].

2.1.2 Active building blocks

P-n junction and diodes The active building blocks are based on the concept of p-n junction-based diodes. The typical U-I curve is illustrated in fig. 1. We can see three different voltage regions. In forward bias mode, the current increases exponentially for an ideal diode. For a real diode, however, there is typically a small series resistor so that the U-I curve approximates the steep linear U-I characteristic of a low-ohmic resistor at high voltages. For the reverse bias, the current saturates until the region of breakdown voltage is reached. This can damage the diode irreversibly. In the forward bias direction, photons are emitted as a result of the recombination of holes and carriers. When there is incident light, the opposite will happen: The absorption of photons results in the formation of a combination of carriers and holes. This effect reduces the effective total current through the device so that the U-I curve is shifted downward for increased intensity of incident light [19]. The following various active components are all based on the p-n junction.

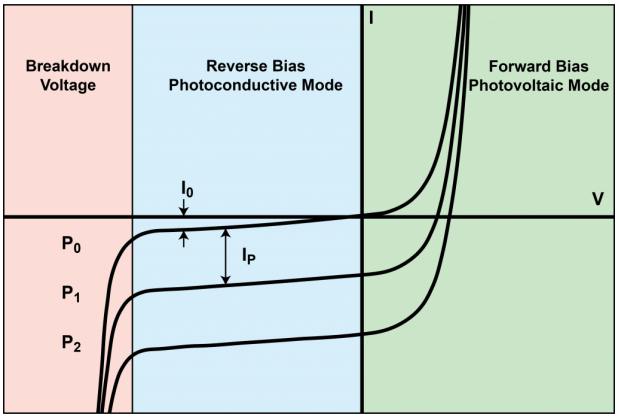

Figure 1: The diagram illustrates the typical voltage-current characteristic of a diode. As the optical input increases, the curve is displaced in a downward direction. The figure is taken from [20].

Distributed feedback lasers (DFB lasers) DFB lasers are used as an optical source and consist of a highly doped p-n junction with an active layer, in which the so-called stimulated emission of the photons occurs. In order to achieve a single-frequency output, there is a grating of a periodically varying refractive index. In this grating, constructive interference occurs only for two counter-propagating waves of a very specific wavelength. This grating works as optical feedback or as a resonator. So contrary to many other laser principles, there are no mirrors necessary for optical feedback. Since there are only those two counter-propagating waves, DFB lasers have a very narrow frequency spectrum and are called single-wavelength lasers. Due to the structure, DFB lasers have two identical outputs. The resonance wavelength of a DFB laser is strongly dependent on the tem-

perature. This can be used to tune the wavelength by cooling or heating [21]. Figure 2 illustrates the working principle of a DFB-laser.

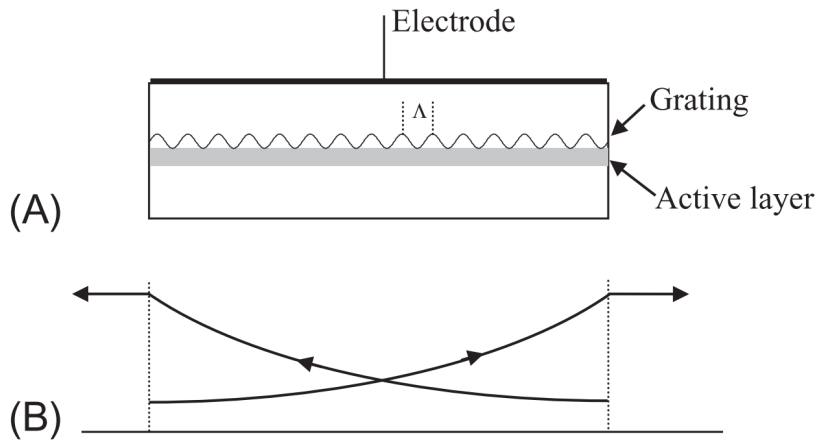

Figure 2: Figure A shows the structure of a DFB laser with grating and active layer. Figure B shows the two counter-propagating waves for which there is constructive interference. The figure is taken from [15].

Semiconductor Optical Amplifiers (SOA) The purpose of SOAs is to amplify light signals. A semiconductor optical amplifier works quite similarly to a semiconductor laser diode, with the decisive lack of a resonator structure: An SOAs also consists of an active medium, the gain medium, but without the grating so that the signal propagates only once through the device. In the active medium, there is stimulated emission by the incoming signal, which occurs in the amplification of this signal [19].

Photodiodes The usage of photodiodes is to measure the power of incident light. As illustrated in fig. 1, the U-I curve exhibits a shift depending on the light intensity. The light intensity can be measured by measuring the photocurrent, since the two are proportional to each other. For DC purposes, measuring the photo current can happen at 0 volts. But for higher frequencies is is advantageous to operate the photodiode with a reverse bias-voltage. The reason for that is that a reverse voltage increases the field in the depletion region which increases the speed of the photodiode [19]. To measure the current, a transimpedance amplifier can be used, which converts currents into voltages.

Electro-absorption modulator (EAM) EAMs are used to modulate the transmitted power by an absorption dependent on the applied voltage which is achieved by utilizing the quantum-confined Stark effect. This phenomenon describes that the effective size of the band gap of a semiconductor material is decreased due to an electric field. A decreased band gap increases the absorption rate of the semiconductor material [21, 15]. Hence, by modulating the applied voltage the absorption of the EAM can be modulated.

2.2 Electronics and High Frequency

2.2.1 Reflection and optimized conduction

When an electrical signal propagates through one conductor and encounters another, reflection occurs at the interface. This reflection is particularly problematic when the line impedances of the different conductors in question differ significantly. The line impedance is a generalization of the concept of complex impedances of electric devices for conductors: For AC-current the line impedance is the ratio of the (complex) voltage and the (complex) current for every point of the conductor. This value depends on the material and the geometry of the conductor. In the event that the line impedance is identical between two conductors or between the conductor and the connected device, reflection is absent. Due to that in field of electronics, it has become standard practice to set the impedance of components and conductors to 50 Ω. For a device that does not have an impedance of 50 Ω, this can be optimized by connecting another impedance as a so-called termination so that the resulting total impedance has a value of 50 Ω [22].

2.2.2 S-Parameters

In order to ascertain the quality of a circuit with regard to optimization for high frequency, it is possible to determine the scattering parameters (S-parameters). For the purposes of this thesis, the S_{11}- and S_{21}-parameters are of primary interest. These parameters are defined for a so-called 2-port which can be a device with an input and an output. The S_{11}-parameter of a device represents the quotient of the amplitude of the reflected wave at the input of a device and the amplitude of the incoming wave at the input. The S_{21}-parameter of a device represents the quotient of the amplitude of the outgoing wave at the output and the amplitude of the incoming wave at the input of the device. The S_{21}-parameter can be determined for the optical output power and the electric output power. Both parameters are contingent upon the frequency applied. Thus, they are determined as a function of frequency to estimate the bandwidth for the device to operate. The S_{11}-parameter also permits the determination of the impedance of a device. [22]. In an optimized circuit, the S_{11}-parameter is expected to be close to zero, as this minimizes reflection. The S_{21}-parameter describing the efficiency of electro-optical modulation requires the translation of the magnitude from the electrical input system and the magnitude from optical output measurements. So often it is normalized to the maximum value (usually DC) to estimate the frequency dependency of modulation since the absolute value does not give relevant information.

2.3 Convolutional acceleration by time-wavelength interleaving

As previously stated, our objective is to implement on-chip a method of convolutional acceleration by time-wavelength interleaving. In this context, convolution refers to the mathematical operation of calculating the convolution of two matrices. This is a computationally heavy task for AI applications. One example is shown in fig. 3 [9]. The figure illustrates an AI classification application where a picture of a handwritten letter shall be classified (there are standardized databases for such classification tasks). For this classification, the feature data is fed into a fully connected layer. But in order to do that,

the feature data has to be generated, and therefore the pixel data (as a matrix of intensities) gets convoluted with different kernel matrices. Those kernels represent different features of the picture. So the resulting data contains information about the edges, the brightness, etc. of the picture. The convolution is mathematically seen as a matrix vector multiplication with variable vectors (the pixel data) and fixed matrices (the kernels). This part of the classification process is rather computationally heavy with a huge amount of operations and computational time for a classical computing architecture [23]. So the goal is to accelerate the whole classification process by accelerating the computationally heavy convolutional operation by doing this computation optically.

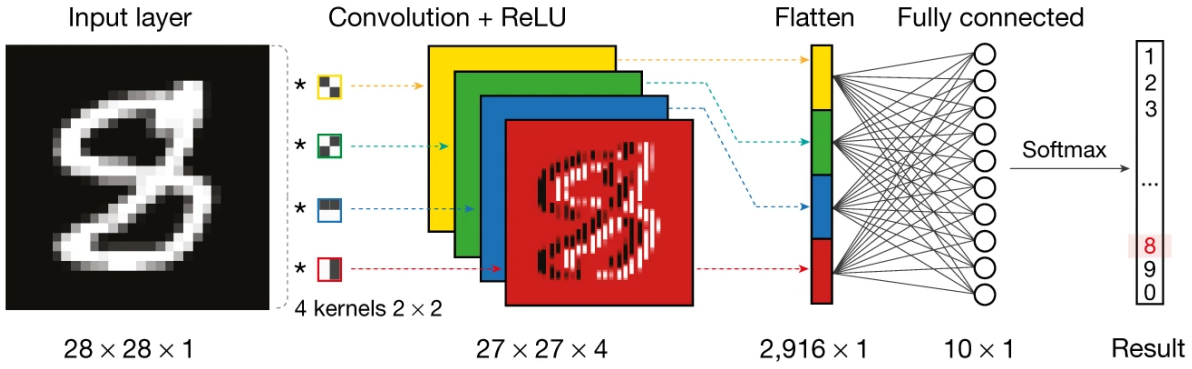

Figure 3: The figure shows the principle of the convolution of a picture with 2x2-kernel matrices. The convoluted data is fed into a fully connected layer. Taken from [9]

One way to perform these convolutional operations optically is the concept of time-wavelength interleaving. The working principle is illustrated in fig. [14]:

For this principle, it is assumed that the objective is to convolute a pixel vector of elements X_{ij} and a kernel matrix with weights W_i . In fig. 3, there is a 4-weight kernel, which corresponds to a 2x2 matrix. The wavelength intensities represent the kernel weights. Subsequently, the wavelengths are multiplexed and transmitted to a modulator, where the input vector is then encoded into the modulation. It shall be assumed that the modulated vector element is X_{ij}, with j indicating the four kernel weights and i indicating the resulting elements of the convoluted feature map. So if the photo diode would be directly behind the modulator the result of the calculation would be $Y_i = X_{ij}W_1 + X_{ij}W_2 + X_{ij}W_3 + X_{ij}W_4$, since all four wavelength intensities are modulated by the same modulation weight X_{ij}. But the relevant calculation would be $Y_i = X_{i1}W_1 + X_{i2}W_2 + X_{i3}W_3 + X_{i4}W_4$. To obtain this result, the different dispersion delays of the different wavelengths are utilized. Between the modulator and the detector, there is a dispersive element through which the signal gets delayed. If the symbol length τ, the time to modulate one symbol, is exactly the same time as the time delay between two neighboring wavelengths due to dispersion, then there happens the right interleaving of the wavelengths. As a result, after four times τ, the calculation at the photo diode behind the dispersive element is actually $Y_i = X_{i1}W_1 + X_{i2}W_2 + X_{i3}W_3 + X_{i4}W_4$. This is at least true for the fourth signal that propagates the dispersive element.The objective is to implement this principle on-chip for one structure of the Laserchip. This will involve multiplexed DFB lasers in place of a frequency comb, as shown in fig. 4, and an EAM in place of the electro-optic modulator (EOM).

If we assume a linear dispersion relation for fibers in a wavelength range around 1550

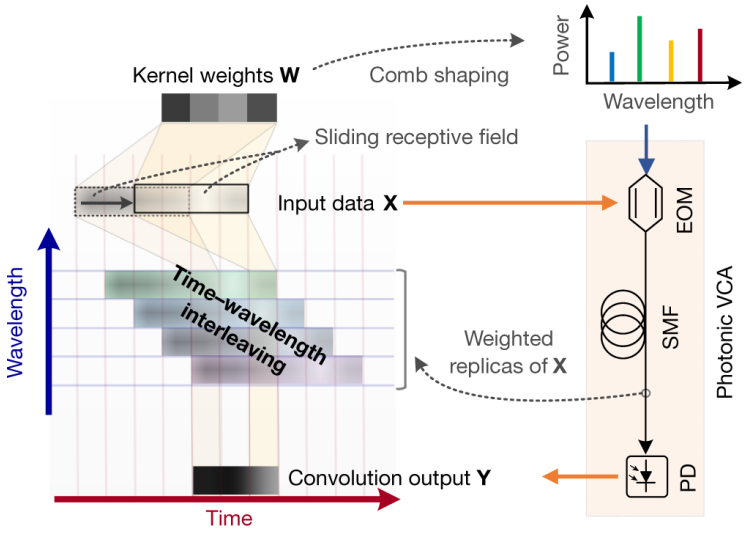

Figure 4: The diagram illustrates the operational method of convolutional acceleration by time-wavelength interleaving. The power of the multiplexed wavelengths represents the weights **W** of the kernel. The modulation (EOM) represents the input vector **X**. The signal propagates through a single-mode fiber (SMF) as a dispersive element. In this dispersive element, the different delay for different wavelengths causes the wavelengths to interleave. Due to that, at the photodiode (PD) the signal represents the correct convolution output **Y**. Taken from [14].

nm, then we require equally spaced DFB lasers with a high degree of precision so that the dispersion delay is correct. Additionally, it is necessary to optimize the modulation frequency of the EAM in order to decrease the symbol lengths τ. The following calculation demonstrates that reducing the length of the dispersive fiber is a requisite step. A typical value, as exemplified in the case of 1550 nm wavelengths, is a delay dispersion of $\Delta T = 17$ ps/(nm km) [14]. Consequently, with the difference in wavelength of two neighboring wavelengths $\Delta\lambda$ the fiber lengths L can be calculated as follows:

$$L = \frac{\tau}{\Delta T \cdot \Delta\lambda}$$

If we assume a $\Delta\lambda$ of 1 nm, a delay dispersion of 17 ps/(nm km) and a modulation frequency $\frac{1}{\tau}$ of 1 GHz, then we get a result of almost 60 km of fiber.

3 Setup

3.1 Photonic chips and printed circuit boards (PCB)

In this thesis, the focus will be on the structures on two InP chips. The following structures are present on the Laserchip and the Detectorchip.

3.1.1 Laserchip

The main structure of the Laserchip is composed of 16 DFB lasers. Since this structure can already be tested on the other structures, this main structure was not considered for testing the active components. Nevertheless, on another PCB, this structure will be bonded in order to have 16 laser outputs for further experiments. Figure 5 shows the GDS schematics of the Laserchip. The two structures that were wire-bonded are marked:

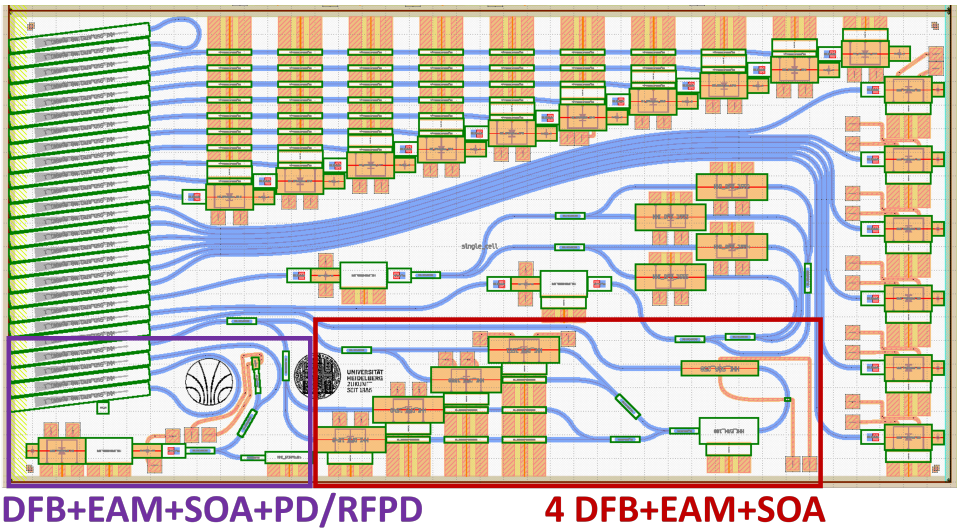

Figure 5: Design of the Laserchip. In the lower left, there is a structure of a DFB-laser with an EAM and an SOA as well as photodiodes. In the lower middle, there is another test structure consisting of four DFB-lasers with an SOA and an EAM.

Four DFB lasers multiplexed The first structure on the Laserchip comprises four DFB lasers, which are multiplexed onto a single waveguide utilizing two MMIs. On one output, the multiplexed light will be amplified and modulated by an SOA and an EAM. On the other output, the beam will be outputted without any modification. The wavelengths of the DFB lasers are designed to be separated by 1 nm intervals, spanning the range from 1548 nm to 1551 nm. With this structure, the objective is to implement convolutional acceleration by time-wavelength interleaving on-chip using the modifiable output of the four DFB lasers. Consequently, the printed circuit board (PCB) for the laser chip was designed in a manner that optimizes the electrical connection of the EAM for high frequency. In the thesis, the four DFB lasers from 1548 nm to 1551 nm are referred to as DFB one to DFB four. Figure 6 illustrates the schematics of this structure.

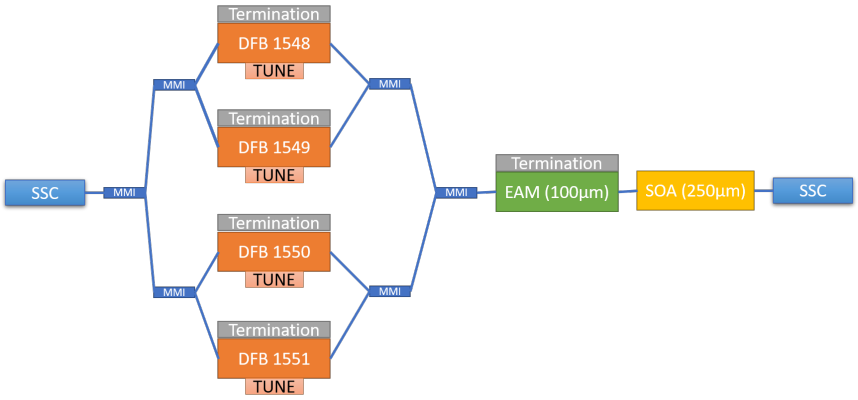

Figure 6: Structure of four DFB-lasers with SOA and EAM

Test structure of DFB-laser with EAM and SOA as well as photodiodes The second structure on the Laserchip is a DFB laser, which is modulated by an EAM and then amplified by an SOA. Furthermore, the signal can be detected by a photo diode and a fast photodiode. The conduction for the fast photodiode and the EAM are optimised for high-frequency applications. Figure 7 shows the schematics.

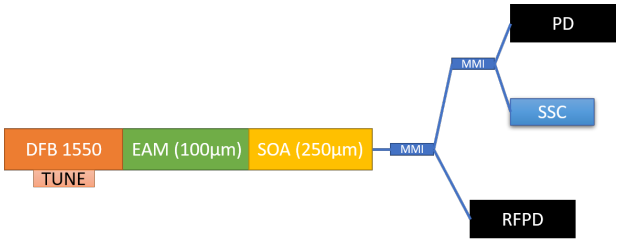

Figure 7: Structure of a DFB laser with an EAM, an SOA and photodiodes as well as a SSC-output

3.1.2 Detectorchip

Schematics of the Detectorchip The main structure of the Detectorchip chip is composed of 16 photo diodes. Figure 8 shows the GDS with the wire-bonded structures highlighted.

SOA and EAM loops The first structure consists of four loops, in which the light is modulated by an EAM and amplified by an SOA. In the thesis, the loops from left to right are referred to as Loop one to Loop four. To test the relevance of high-frequency optimization, the third and fourth EAMs are terminated with a 50 Ω resistor, while the other two EAMs are not terminated. On the PCB, the first and fourth connections of the EAM are optimized in terms of conduction geometry, in contrary to the other two EAMs. Figure 9 illustrates the structure of the loops.

DFB with SOA or EAM including photo diodees This structure contains a DFB-laser with one output, including an EAM, and one output, including an SOA. For both

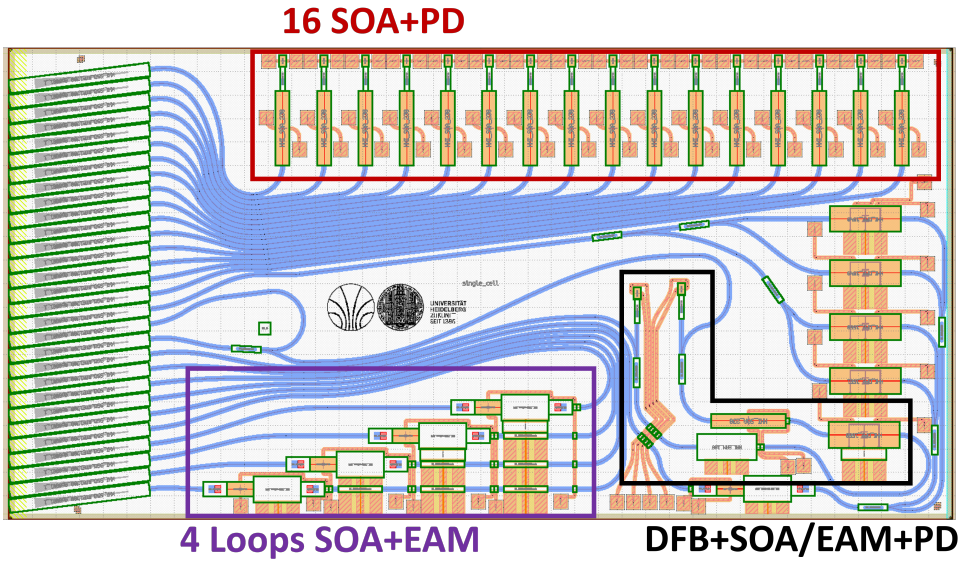

Figure 8: Design of the Detectorchip. In the lower middle there is a structure of four loops, in the upper right there is the main structure of 16 photodiodes, and in the lower right there is a structure of a DFB with an output with an EAM and another output with an SOA.

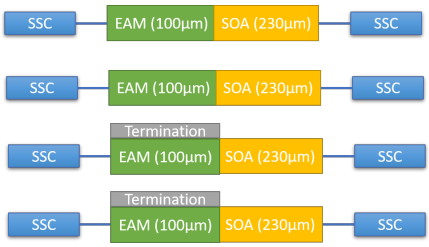

Figure 9: Structure of four loops with SOA and EAM

structures, the optical signal is transferred to a photodiode via an MMI. In this structure, both the EAM and the DFB are not terminated, but the conduction is optimized for both. The schematic of this structure is presented in fig. 10:

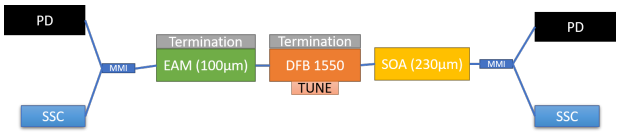

Figure 10: DFB-laser with one SOA and one EAM output, including photodiodes

16 photodiodes, including amplification The most important structure of the Detectorchip comprises 16 photo diodes with a pre-amplification by SOAs, whose schematics is shown in Fig. 11.

Figure 11: 16 photo diodes with SOA

For high-frequency applications, it is advantageous to AC-couple the photodiodes using a resistor and capacitors and apply a negative bias voltage. The circuit for the connection of the photodiodes is shown in Fig. 12.

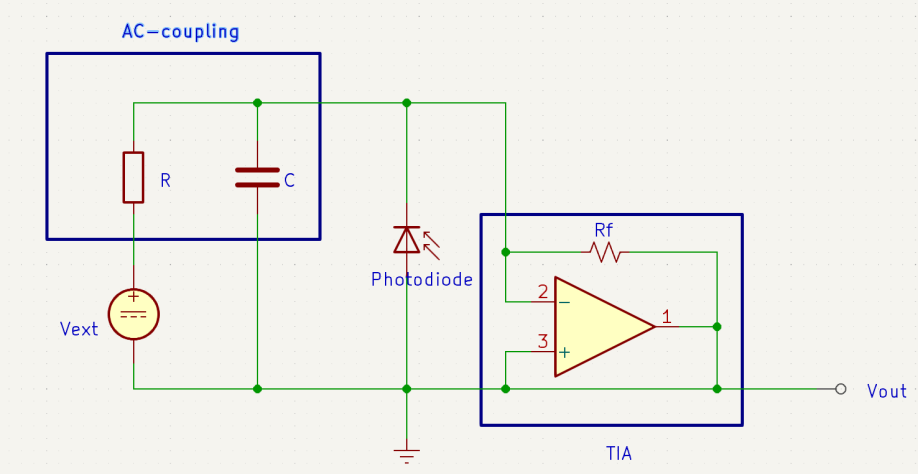

Figure 12: Circuit diagram for the 16 photo diodes with AC-coupling

3.2 Printed circuit boards (PCB) and wire-bonding of the chips

PCBs are used as the carriers for the chips, and they establish the electrical connection to the chips via wire-bonding. The chip is positioned on the PCB with the SSCs facing the edge. For the purpose of providing an electronic connection between off-chip devices and the PCB, SMA or pin connectors will be employed. Some of the conductions on the PCB need to be optimized to a waveimpedance of 50 Ω. Hence, it is essential to follow the specified geometry provided by the PCB manufacturer for optimized conduction, which is, in that case, the geometry of a coplanar waveguide.

Figure 13 illustrates the 3D model of both PCBs while fig. 14 shows how the Detectorchip looks when wire-bonded. Figure 14 shows an image of the Detectorchip wire-bonded on its PCB.

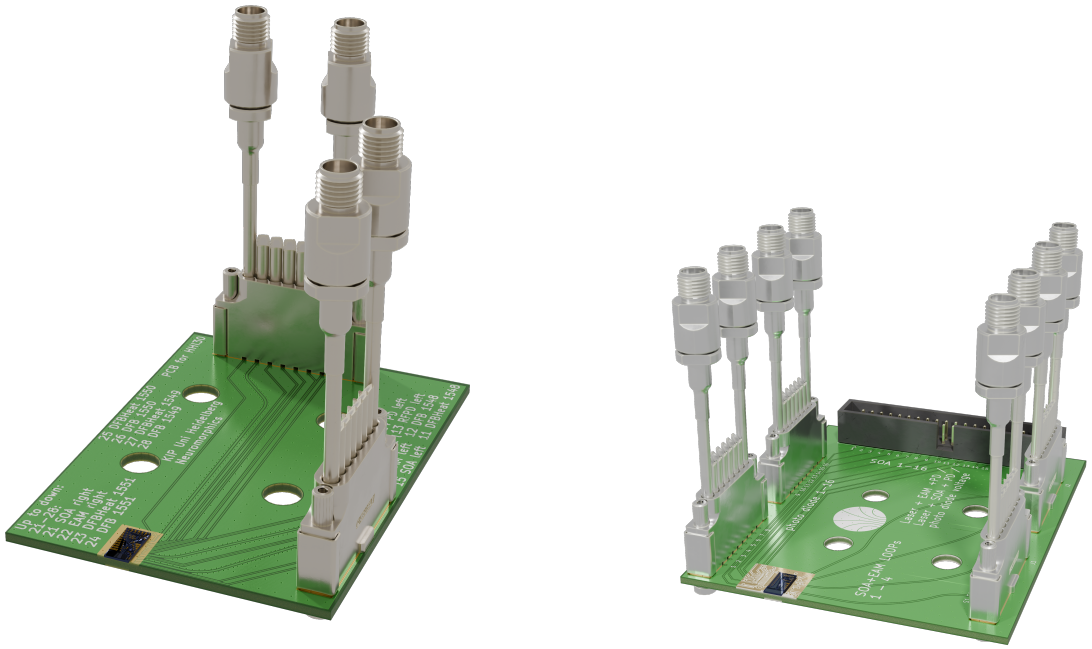

(a) Design of the Laserchip (b) Design of the PCB for the Detectorchip

Figure 13: The figures show the 3D model of the PCBs for both chips. The model illustrates the four mounting holes used to fix the PCB to the rotational stage, the conduction paths on the surface, the InP chip positioned at the front edge of the PCB, and the SMA connectors, along with the pin connector for the detectorchip.

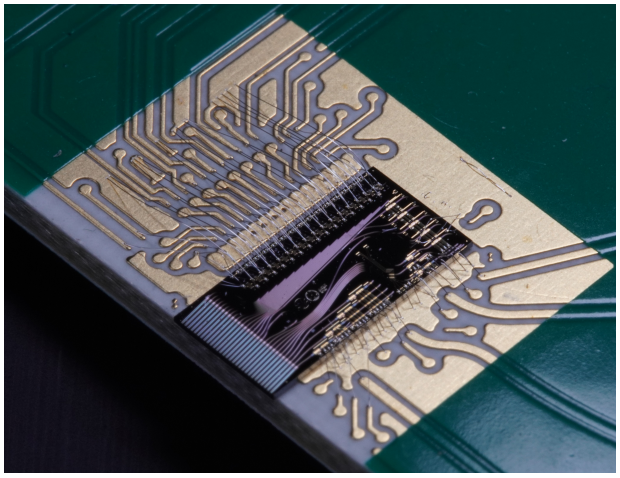

Figure 14: The figure shows the Detectorchip and the fine wires that connect the printed circuit board (PCB).

3.3 Experimental setup and optical interfacing

The optical setup for the majority of the experiments consists an InP-chip wire-bonded on a PCB and a fiber array, which enables the optical interfacing of the chip. In order to achieve this, the fiber array must be brought into close proximity (approximately 40 µm) to the SSCs. Consequently, the PCB is mounted on a rotational stage, while the fiber array

is positioned on a hexapod, which is capable of making changes in position and rotation within the micrometer range. A microscope camera is positioned above the entire setup in order to ascertain the distance between the chip and the fiber array to prevent accidental crashes of the chip and the hexapod. Figure 15 shows this basic setup.

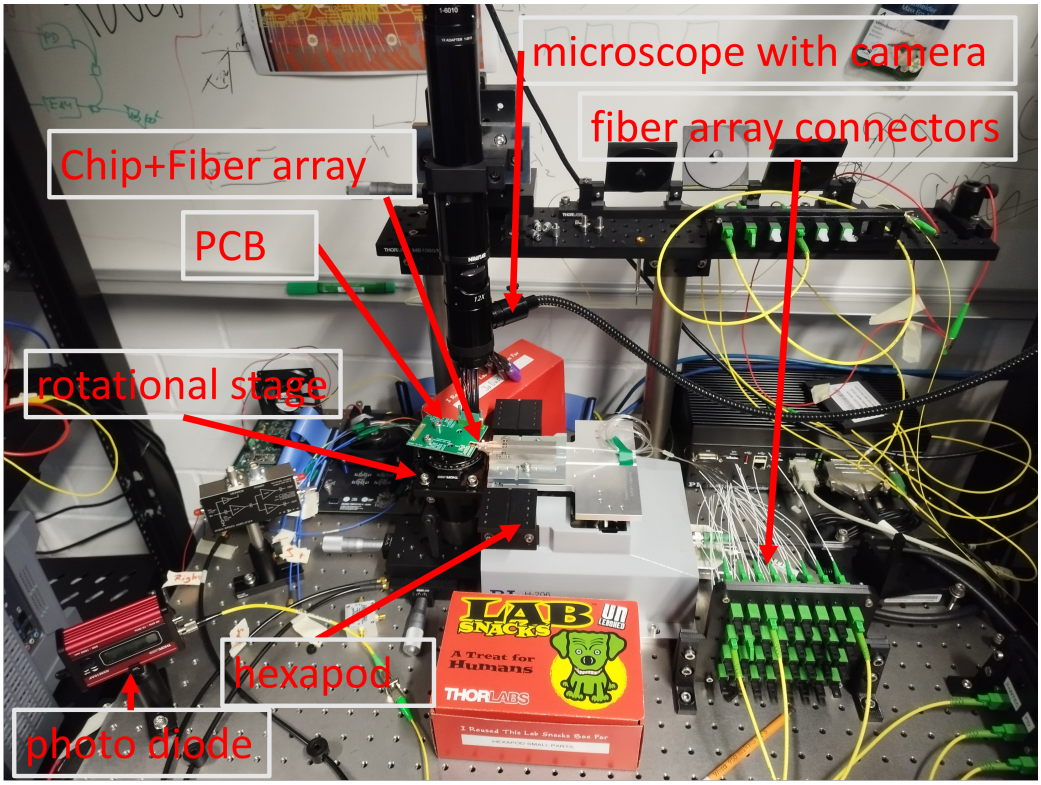

Figure 15: Picture of the schematic view of the basic optical setup. In the middle, there can be seen the rotational stage with the PCB and the InP-chip on top of it next to the hexapod and the fiber array. In the lower right, there are the connectors for the fiber array which allows the optical interfacing of the chip. Above the PCB there is the microscope. In the lower left, there can be seen an external photodiode.

A picture of PCB, Laserchip and fiber array under the microscope can be seen in fig. 16 a).

In situations where the objective is to achieve the greatest possible coupling efficiency, rather than the ability to switch between different SSC outputs, it is beneficial to couple with a single-mode fiber, as illustrated in the fig. 16 b).

In the appendix, there is a description of all other experimental devices that were utilized for this thesis.

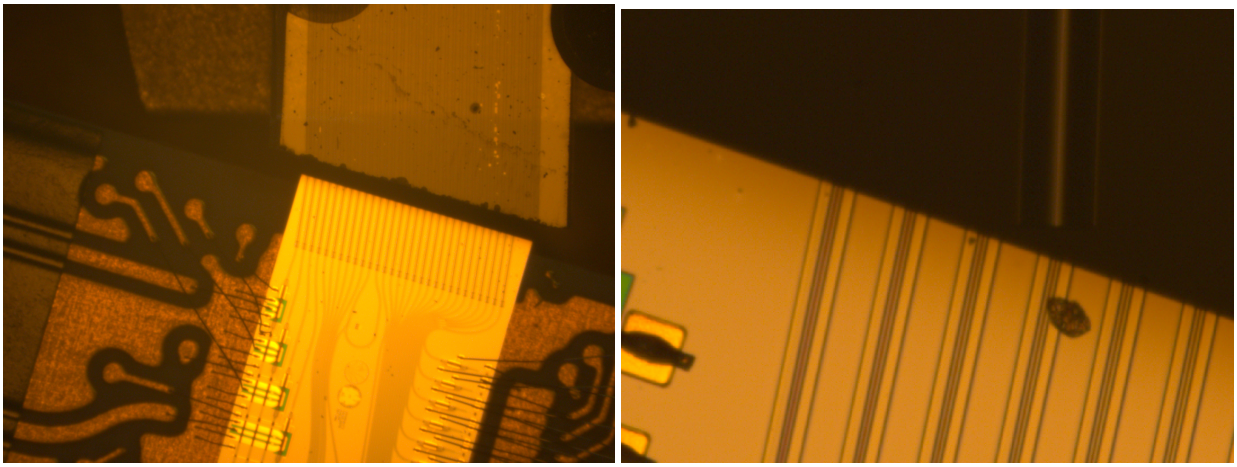

(a) Coupling with the fiber array (b) Coupling with a single-mode fiber

Figure 16: Figure a) shows the Laserchip and the fiber array from the perspective of the microscope. At the interface between the fiber array and the chips, it is possible to observe the SSCs on the chip and the fibers within the fiber array. Figure b) illustrates the coupling through SSCs and a single-mode fiber.

4 Experiments

4.1 Alignment and coupling loss

One of the most significant challenges encountered during the experimental phase was the necessity to align the chip and the fiber array optimally. This was essential to minimize loss and increase the intensity of the signal. Therefore, before conducting the actual tests of the building blocks, it is important to consider the coupling loss and the alignment.

4.1.1 Coupling loss dependency on distance

Given that the coupling loss is dependent on distance, it is advisable to minimize the distance between the fiber array and the chip. Nevertheless, it is important to prevent a crash, as both the hexapod and the optical chip are highly sensitive to damage. So it is necessary to identify the optimal distance at which the fiber array should be positioned.

To quantify the distance-loss-dependency, one laser output was aligned at an estimated distance of 40 µm between fiber and chip and the intensity was measured . Figure 17 shows the resulting dependency:

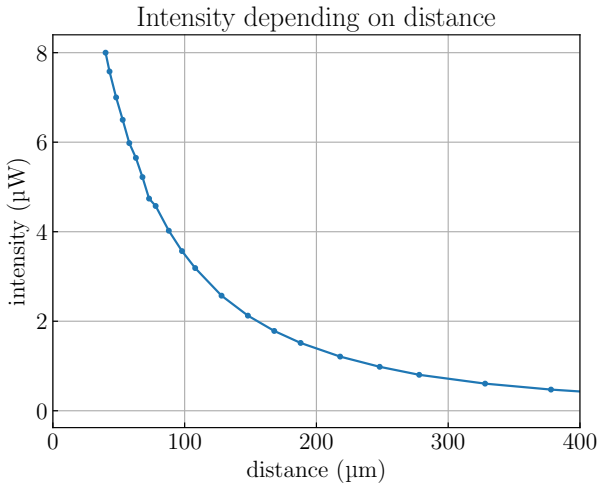

Figure 17: The figure illustrates the measured intensity for increasing distances. The shown distance is for optimal alignment for a given distance, so the fiber array was first moved in the x-direction and then the y-direction was corrected for optimal alignment for the given distance.

The theoretically determined overlap integral for this configuration for coupling is shown in fig. 18.

This theoretical dependency was calculated under the approximation of a Gaussian beam for the given size of the single fiber mode and the size of the mode in the SSC.

It is expected that the graph of the overlap integral and the experimental dependence of the intensity will show similar trends. This can be verified qualitatively by comparing the two graphs. The overlap integral indicates that at a distance of approximately 40 µm, the measured intensity has already reached 80 % or -1 dB, of the maximal power that could be gained by decreasing the distance. Given the difficulty of preventing crashes and the time required to align at shorter distances, it was decided that 1 dB additional loss due to

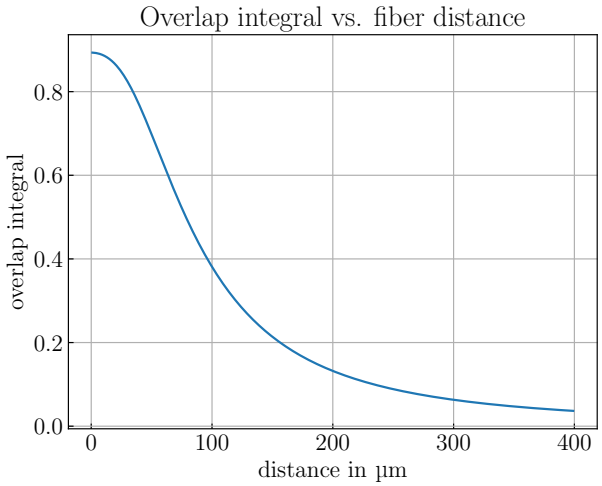

Figure 18: The graph illustrates the theoretically calculated overlap between the SSC mode and the fiber mode for a specified distance.

distance is acceptable, so that the typical coupling distance for the following experiments was around 40 µm.

4.1.2 Loss on the optical path and alignment loops

In order to determine the coupling loss, the alignment loops on the chips were used. Alignment loops are structures consisting solely of two SSC connectors linked by a waveguide. Therefore, for an alignment loop, the only relevant loss is approximately twice the coupling loss.

To ascertain the optical loss associated with the coupling, it is necessary to first determine the loss incurred by all the devices and connectors that constitute the optical path. When the external laser source is connected directly to the fiber array, then the resulting loss was -2.4 dB comparing the output power of the external laser source and the measured power in the power meter

For estimating the loss of the fiber array, the external laser source is connected to one of the outputs of the fiber array, while the free-space powermeter measures the intensity that reaches the input of the fiber array. The loss of the fibers is between -1 dB and -4 dB, although the majority of the losses are concentrated around the median loss of -2.1 dB.

The total loss for an alignment loop when comparing laser power and the measured power in the powermeter was estimated to be -17.5 dB.

The loss of the optical path for the alignment loop consists of the loss measured when the laser was connected directly to the power meter, which was determined to be -2.4 dB. Additionally, the loss includes twice the -2.1 dB loss of the fiber array. Therefore, the total loss of the surrounding optical path is calculated as follows:

$$-2.4\,\mathrm{dB} + (-2.1\,\mathrm{dB}) + (-2.1\,\mathrm{dB}) = -6.6\,\mathrm{dB}$$

As a result, the combined loss for in-coupling and out-coupling to the alignment loop is calculated as follows:

$$-17.5\,\mathrm{dB} - (-6.6\,\mathrm{dB}) = -10.9\,\mathrm{dB}$$

Thus, the single coupling loss is determined to be approximately:

$$\frac{-10.9\,\mathrm{dB}}{2} = -5.5\,\mathrm{dB}$$

A way to reduce the coupling loss is to couple with a single-mode fiber, as previously mentioned. This method enables a doubling of the intensity, thus reducing the coupling loss to around -3 dB. The reason for this is that the distance between the SSC and the single-mode fiber could be further reduced.

It was demonstrated that it is essential to achieve the closest possible proximity between the fiber array and the chip. Therefore, it is crucial that the chip is positioned slightly beyond the edge of the PCB. For a first try with one of the Laserchips on a PCB, the chip was behind the edge of the PCB, resulting in a minimal coupling distance of approximately 150 µm and a coupling loss that was significantly higher than -10 dB.

4.2 DC single operation of all active components

Once the optimized alignment was achieved, it became possible to characterize all the building blocks, initially in DC mode.

4.2.1 DFB-Laser

Laser spectrum One of the important reasons to use InP-chips is the possibility of on-chip integration of laser sources. Hence, the spectrum of DFB lasers needs to be examined.

The optical spectrum analyzer (OSA) is used to determine the spectral power density of one of the DFB lasers. Figure 19 illustrates the spectra of a DFB laser with a designed peak wavelength of 1548 nm for different laser currents.

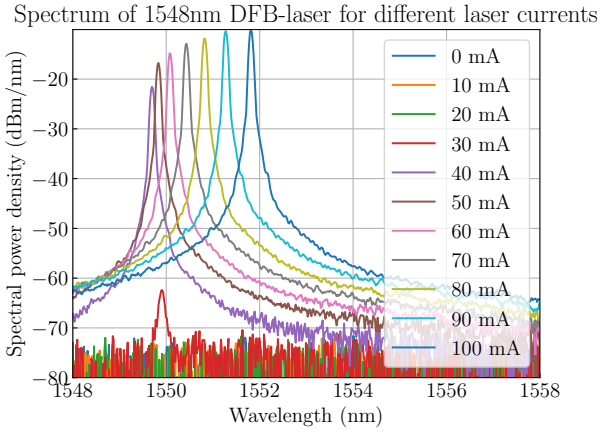

Figure 19: The figure illustrates the wavelength spectrum for a designed 1548 nm DFB laser for different laser currents.

For this set of chips the peak wavelengths deviate by approximately 3 nm from the designed wavelength, which can be seen in fig. 19. The graph shows that the power of the

peak is strongly increasing with an increase of current up to 40 mA until the threshold voltage is exceeded. Then the power increases linearly and later exhibits saturation.

A shift in wavelength can be observed when increasing the current. This phenomenon can be attributed to the linear dependence of the wavelength of the DFB laser on temperature. As the current increases, the temperature also rises.

Current-voltage characteristic While examining the applied current, it is essential to consider that the actual current in the DFB laser is lower due to a parallel resistor of 50 Ω as a termination (in our fabrication, the termination resistors were measured with a value of rather 65 Ω). Figure 20 shows the comparison of the U-I curve for a laser with and without termination.

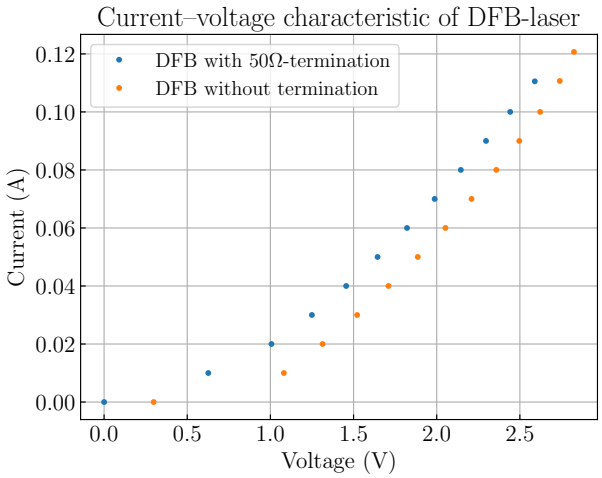

Figure 20: The graphs illustrate the current-voltage characteristic of two DFB lasers. One of them is terminated, and the other is not.

It is evident that both curves exhibit the characteristic shape of a forward-biased diode curve. The distinction is that at low voltages, the slope of the U-I curve for the laser with termination is steeper since the laser is still below the threshold. So for the laser without termination there is almost no increase in current while for the laser with a termination of a parallel resistor the increase of current is mainly due to current through this resistor. For higher voltages, the typical shape of the current-voltage characteristic of a diode can be observed in both curves. At voltages higher than the anticipated threshold voltage of roughly estimated 1.5 V, the predominant component of the U-I curve is the series resistance of the laser diodes, which is estimated to be approximately 15 Ω.

Total power of the lasers To determine the total power of the lasers, a free-space power meter was utilized. Hence, the light-sensitive area of the free-space power meter is put directly in front of the SSCs so that almost all emitted light on-chip gets detected. The total power was between 2 and 3 mW for applied currents between 70 and 100 mA. For a chip from a different wafer, the total output power was slightly lower, at approximately 1 to 2 mW. These values are consistent with the expected values.

Equal spacing of DFB-lasers As previously observed, the peak wavelength of the DFB lasers can deviate more than 3 nm from the designed wavelength. Therefore, it was necessary to ascertain whether the wavelength deviation was consistent for all lasers on a single chip. Hence, the peak wavelengths of the four DFB lasers were compared. The lasers are designed that the wavelengths will fall within the range of 1548 nm to 1551 nm, with a spacing of 1 nm between each value. Figure 21 illustrates the peak wavelengths of the four DFB lasers for varying currents.

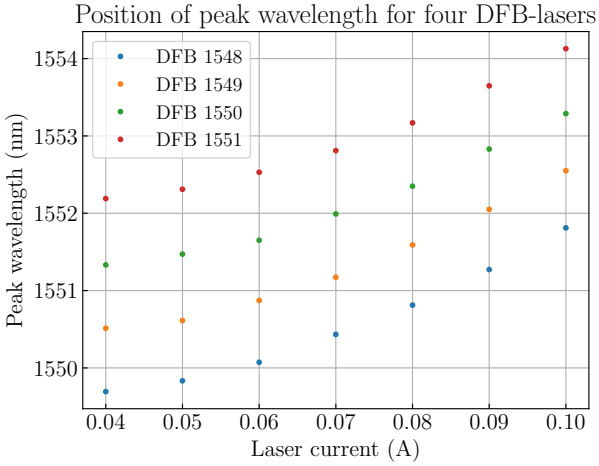

Figure 21: The figure illustrates the wavelength of the peak of the four DFB lasers in relation to the laser current. Above 30 mA, the spacing of the peak wavelengths is observed to be quite equidistant.

It can be observed that for currents exceeding approximately 30 mA, the peak wavelengths deviate agian around 3 nm from the designed range, but that the peak wavelengths are distributed in a relative uniform manner. The spacing is less than 1 nm, but rather 0.8 nm. In a second fabrication, the spacing of the lasers was found to be correct as 1 nm, but for this fabrication, the deviation from the designed wavelength was even 7 nm. So the wavelengths appear to deviate significantly from the designed value. However, across the entire chip, the offset is consistent. Thus, the relative wavelength remains relatively reliable.

4.2.2 DFB-Tuning

In certain applications, it is necessary to have a specific wavelength value. It is therefore of interest to be able to alter the wavelength of the DFB lasers. Hence, the objective is to assess the functionality of the DFB tuners. As anticipated, the U-I curve of the heaters exhibited a linear shape of Ohm's resistors. A linear fit yielded a resistance value of 20–27 Ω.

In order to determine the tuning range, it was necessary to determine the maximum voltage that could be applied to the resistor without damaging it. Therefore, it was tested to apply 1.8 V at a current of approximately 100 mA for half an hour to one of the resistors. The outcome of this experiment was that the U-I curve remained unchanged, which led to the conclusion that it is safe to apply a voltage of up to 1.8V to the heaters. Figure 22 illustrates the effect of tuning a DFB laser.

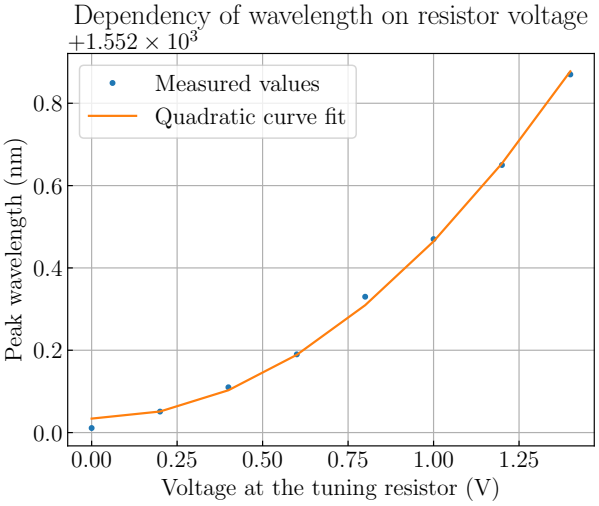

Figure 22: The figure illustrates the dependence of the peak wavelengths in relation to the applied voltage at the tuning resistor. It can be seen that a voltage of up to 1.4 volts allows for a tuning of up to 0.9 nm. The curve fit indicates that the dependency on the resistor voltage can be approximated by a quadratic function, as was expected.

As can be observed, the tuning range extends up to 0.9 nm when voltages are applied up to 1.4 volts. As the resistors were tested for voltages up to 1.8V, the tuning range is therefore even higher. However, for the intended applications, a tuning range of around 1 nm should be sufficient, given that the laser spacing is also only 1 nm. Figure 22 shows also a quadratic fit (including a constant offset) through the data points, which appears to represent the data adequately. The reason for that is that the electric power of the resistor is proportional to the square of the voltage. It is anticipated that the wavelengths of the lasers are proportional to the temperature. Assuming a linear dependency of the heat power and the temperature (which is equivalent to the assumption of a constant heat capacity for the DFB laser), it can be concluded that the dependency of the wavelengths on the applied heat voltage is also quadratic.

It is important to note that the generation of heat by each current on the chip affects the wavelengths of all lasers. Thus, it is necessary to identify a steady state for each configuration of operational devices on the chip.

In conclusion, the DFB lasers appear to function as anticipated. The absolute wavelength may differ significantly from the designed value, but the relative wavelengths appear to be quite consistent. Furthermore, the total power reaches up to 3 mW, and the wavelength tuning range extends up to 1 nm.

4.2.3 Electric absorption modulators (EAM)

Spectrum and modulation range In order to determine the effect of different modulation voltages applied at the EAM, it is necessary to record spectra on the OSA for different voltages.

Figure 23 illustrates that the optical power decreases with a decrease in the applied voltage. At a voltage of around -1V the power starts to saturate and the spectra exhibit only minimal variation with further decreases in voltage. As illustrated in the plot, a red

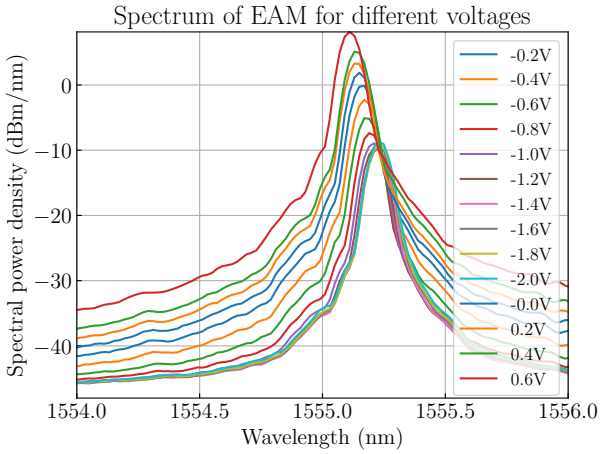

Figure 23: The figure displays the laser spectra for varying EAM modulation voltages. A subsequent SOA was operated at a current of 50 mA.

shift in wavelength is observed for lower voltages. This phenomenon can be explained by the rise in current through the EAM as voltage is decreased, which in turn leads to an increase in temperature and a corresponding shift in wavelength.

Given that all of the EAMs on our chips have a length of 100 µm, it can be assumed that they should all function in a similar manner. Nevertheless, it appears that the modulation voltage differs between different EAMs. Figure 24 illustrates the modulation range for two EAMs. The curves show the spectral power density of the peak wavelengths plotted against the applied modulation voltage at the EAM.

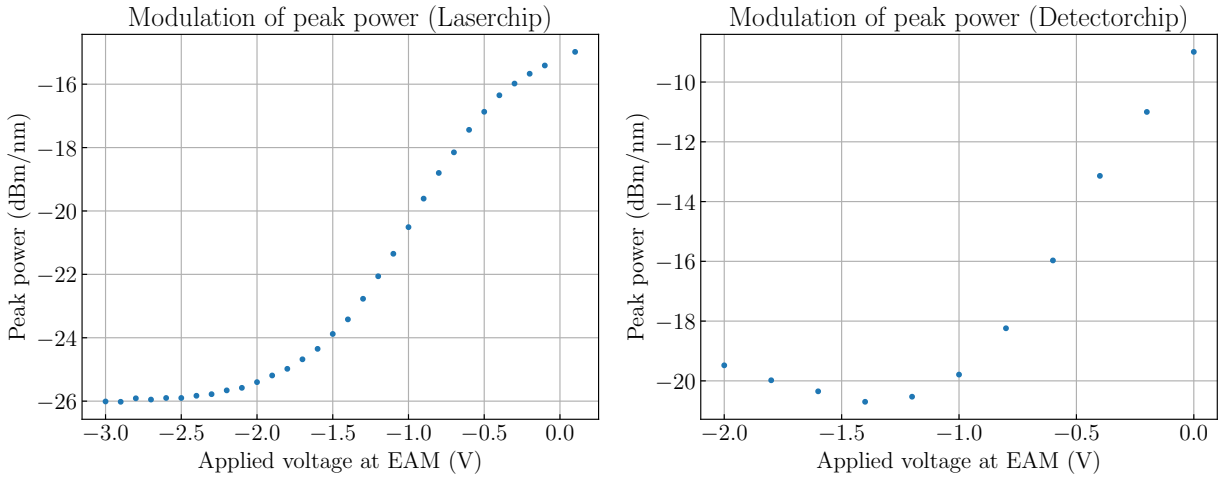

(a) (b)

Figure 24: The figure shows the peak power for different voltages applied at an EAM. Both devices exhibit a modulation of the peak power of approximately 10 dB. However, the EAM on the detector chip reaches saturation at a voltage of approximately -0.5 V. The saturation point of the other EAM is approximately 0 V.

In one case, saturation is observed at approximately -0.5V, while in the other, it occurs at 0V. In the context of modulation, it is beneficial to have a voltage region that exhibits a

linear dependency on the modulation voltage rather than a region of saturation. Therefore, it appears necessary to determine the modulation region for each EAM individually. The modulation range for both EAMs is approximately 10 dB. Additionally, comparison values for the InP-based chips from the Heinrich Hertz Institute were found for the EAMs. These results are similar to those obtained here [16].

It is also of interest to examine the dependency of the modulation on the wavelength. Hence, the EAM of one of the SOA+EAM loops from the detector chip was tested at wavelengths of 1550 nm, 1555 nm, and 1560 nm with the same intensity. The result is shown in fig. 25.

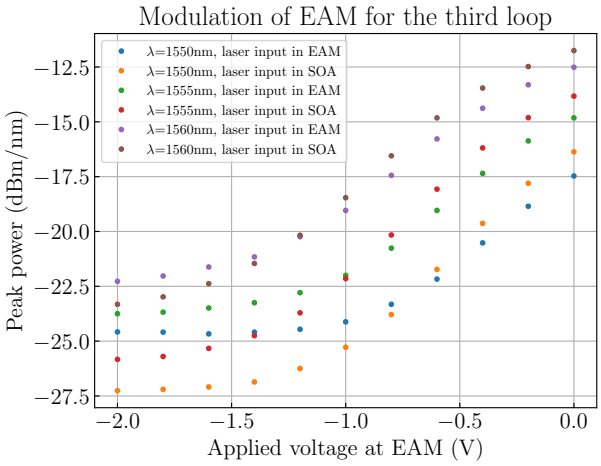

Figure 25: The figure shows the peak power for the third loop on the detector chip. The modulation was conducted for three distinct wavelengths, and it was tested whether there was an effect if the optical power goes first into the SOA or first into the EAM. The SOA current was always 100 mA.

As illustrated in the graph, the absorption is greater for shorter wavelengths, which is also consistent with our expectations. The modulation range is slightly higher when the optical power is initially directed into the SOA and subsequently into the EAM. But it has to be noted that for one of the loops, it was the opposite, and for another one, it did not make a difference which of the components was put first in the optical path regarding the modulation range.

The main difference between both orders is that when the SOA is put first, then the EAM also modulates the SOA noise. Vice versa, there is a constant offset of the SOA noise in the optical spectrum, as can be seen in fig. 23. But that should not affect the peak power, which would be consistent with the observation.

Even when no voltage is applied, the EAM has an intrinsic insertion loss that is expected to be approximately -6 dB. This value was found to be consistent with intensity measurements on the chips.

Current-voltage characteristic of an EAM Some of the EAMs are terminated with a parallel resistor of a designed value of 50 Ω (the termination resistance is anticipated to be approximately 65 Ω). This will also affect the current-voltage characteristic of the EAMs. Moreover, for the EAM the U-I characteristic also depends on the optical input into the EAM, as evidenced by fig. 26 a).

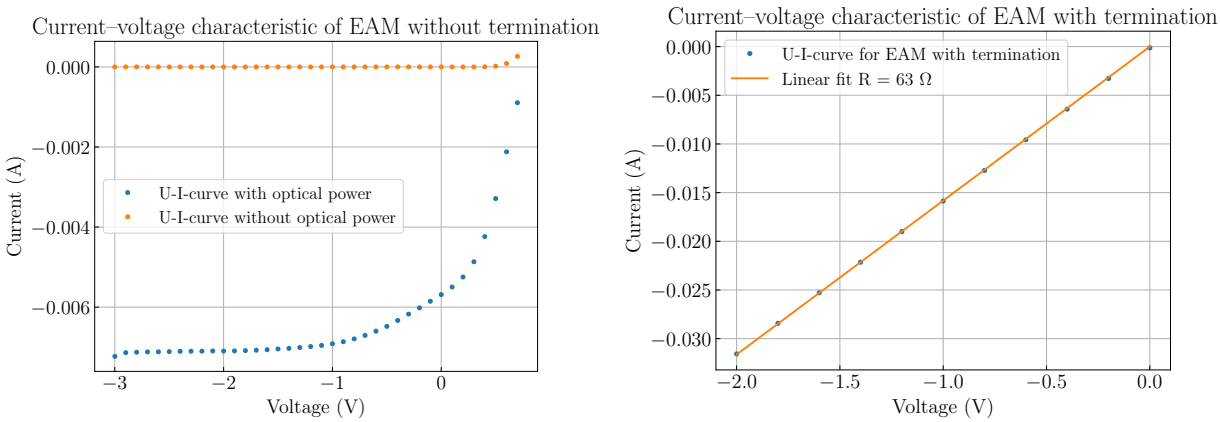

(a) (b)

Figure 26: The two figures illustrate the current-voltage characteristic of EAMs. The two graphs in a) are from an EAM without termination, but one with light input, the other without optical input. The graph in b) is from an EAM with a parallel resistor as termination. The current-voltage characteristic can be attributed to that of an ohmic resistor, as evidenced by the well-fitting linear curve fit.

The figures for the EAMs without termination exhibit a clear reverse-biased diode curve. The current reaches a saturation point at increasing negative voltages. The leakage current for the EAM with optical power is greater than that without optical power.

In the case of the EAM with a termination resistor, the current-voltage characteristic is almost perfectly linear. A linear curve fit indicates a resistance of 63 Ω. For a terminated EAM the effect, with or without optical power, was negligible in the U-I curve. This is consistent with expectations, given that in reverse bias, the leakage current is negligible compared to the current flowing through the termination resistor.

To conclude, the DC measurements with the EAM indicate a modulation range of 10 dB for a length of 100 µm. It appears that the voltage range suitable for modulation varies between identical EAMs. Therefore, it is essential to determine this voltage range for each EAM individually.

4.2.4 Semiconductor optical amplifier (SOA)

Spectrum and amplification range SOAs are on-chip devices used to enhance the intensity. In order to assess the functionality of SOAs, a test structure on another InP-chip of the same fabrication run as the Laserchip and the Detectorchip is used. The schematics of this structure are shown in Fig. 27.

As illustrated in Fig. 27, the structure consists of a loop with a single input and two outputs. One of the structures contains an SOA with a length of 400 µm within the optical path. The advantage of this structure is that it allows for the direct comparison of the effect of the SOA to that of an identical optical path without an SOA. A constant external laser input signal results in the spectrum, shown in Fig. 28 for different SOA currents.

It can be observed that the SOA functions as a current-dependent offset for the laser spectrum. The wavelength remains unaltered, although it is evident that the heat produc-

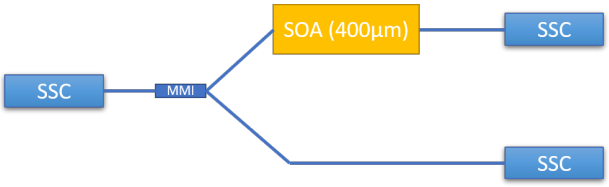

Figure 27: This structure comprises a loop with one input and two outputs. One output includes an SOA, the other does not.

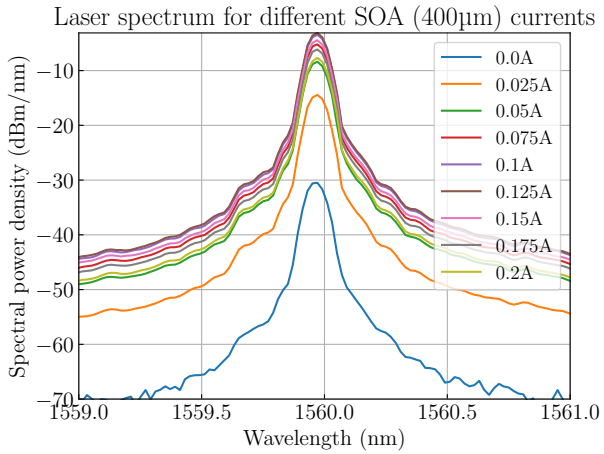

Figure 28: The figure shows the spectra of the SOA for different amplification currents. The input laser signal originates from an external laser source with a wavelength of 1560 nm.

tion of the SOA affects the wavelengths of the DFB lasers when they are integrated on a chip.

The plot in fig. 29 a) shows the peak power of the spectra, together with the peak level of the noise spectra of the SOA and the peak power of the spectra of the reference optical path:

The maximum gain of the SOA is the difference between the power of the reference path and the maximum power of the SOA sweep. This value is approximately 10 dB, which is consistent with the anticipated outcome. The maximum gain is observed for a current of approximately 120 mA, which is also consistent with the expected saturation at around 100 mA.

The propagation loss when the SOA is not pumped can be determined by the difference between the peak power of the reference path and the peak power of the SOA with zero current. This value is approximately 20 dB, which is higher than the estimated value of 12 dB.

A further test was conducted to determine whether there were significant discrepancies between the curves of the peak power and total power. Both curves are quite similar in their shape.

One disadvantage of amplifiers in general is that they produce noise, which reduces the signal-to-noise ratio of the amplified signal. In order to calculate the signal-to-noise ratio,

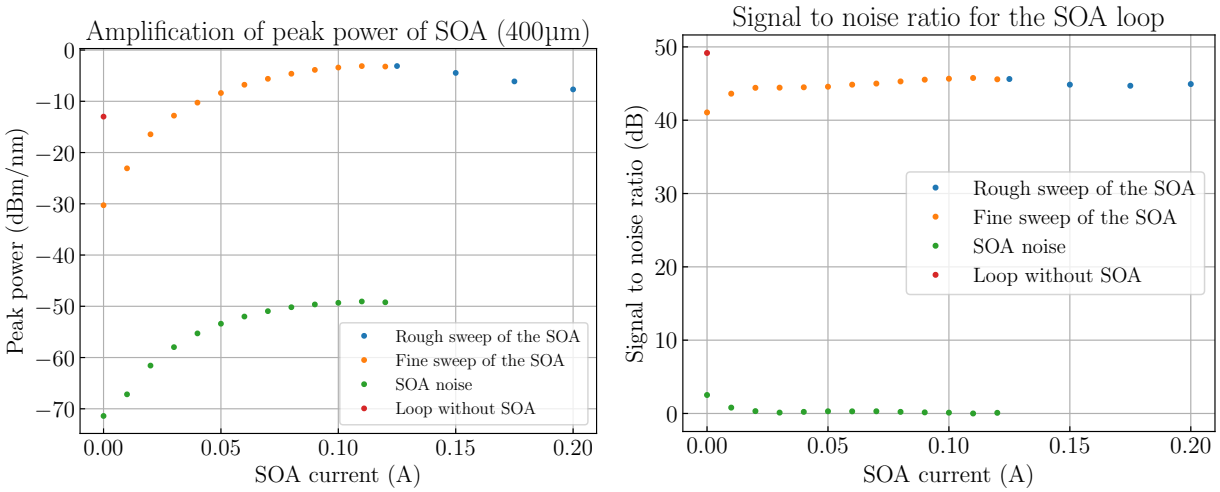

(a) (b)

Figure 29: Figure a) illustrates the amplification of the peak power for the SOA in the test loop. The blue and orange values represent the results of a rough and fine sweep of the SOA current with laser input. The red measurement value represents the peak power of the optical path without the SOA, while the green points indicate the peak power of the noise generated by the SOA when the laser is turned off. Figure b) shows the calculated signal-to-noise ratio

the difference is formed between the peak power in the optical spectrum and the maximum of the noise level before the peak. Figure 29 b) shows this ratio for the same measurement as fig. 29 a).

It is expected that the noise figure, which is the difference between the signal-to-noise ratios of the optical path with and without SOA, will be approximately 7 dB. The data is consistent with that since the difference in the signal-to-noise ratio is between 5 and 10 dB. Note that the signal-to-noise ratio for the noise is almost zero. This means on a logarithmic scale the 'signal' and noise are of the same magnitude, which should be the case for a noise signal by definition.

The previously considered SOA has a length of 400 µm, whereas all the SOAs on the laserchip and the detectorchip have a much shorter length of 250 µm or 230 µm. That has to be taken into account for the following experiments:.

Figure 30 illustrates the amplification of peak power for an SOA for different SOA currents maintained at a constant laser current:

It can be observed that there is an early saturation in power and a decline in amplification for higher currents. The peak power for 250 mA is almost at the same power level as the value for zero current. The earlier saturation is consistent with expectations, given that this SOA is almost half the length of the 400 µm long SOA. However, the early and strong decrease in amplification, rather than a real saturation, is contrary to expectations. One possible explanation for this phenomenon is that the increased current has led to a significant rise in heat generation, which might affect the amplification. To test the effect of the heat, it could be interesting to operate the SOA with cooling applied so that it remains at a constant temperature.

As there was no reference structure, it is challenging to estimate the precise gain of

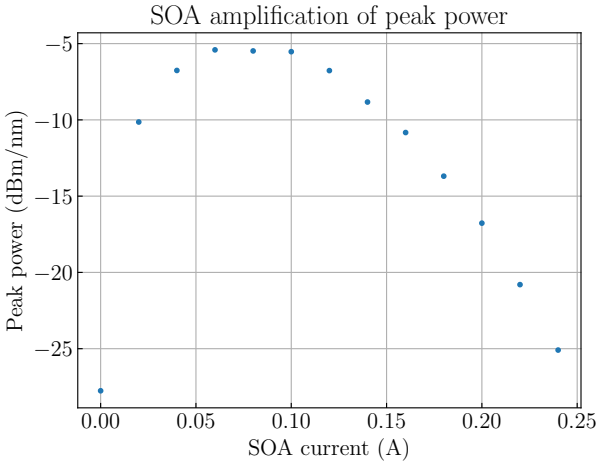

Figure 30: The figure illustrates the amplification of an SOA for different currents. This SOA is 250 µm long, so it exhibits the saturation point earlier than the 400 µm long SOA.

the shorter SOAs. Assuming a linear relationship between amplification and SOA length, it would be expected that the shorter SOAs would amplify by 3-5 dB, which is consistent with the majority of the conducted measurements.

Nevertheless, at least one of the SOAs seemed to have, even when pumped, a higher absorption than amplification. That was observed for the structure on the Detectorchip with one laser having two outputs, one including an SOA and the other including an EAM. The optical path of the SOA included also one MMI which causes an extra loss of -4 dB, but the EAM is expected to have an insertion loss of around -6 dB without an applied voltage. So one would expect the SOA output to be higher even when the amplification of the SOA was just as high as the absorption. But even for an optimally pumped SOA and an open EAM, the optical output of the EAM path was higher than that of the SOA output. It can be concluded that the short SOAs are not fully reliable in their amplification.

Furthermore, the SOAs of the detector chip loops were tested for different wavelengths, which resulted in the graphs shown in fig. 31 a).

The plots demonstrate that the amplification is slightly higher when the optical power is initially directed into the EAM and when the wavelength is larger. For the SOA, it is anticipated that the wavelength dependency around the peak wavelength will exhibit a greater amplification for higher voltages. But this is rather significant on larger wavelength scales. In a range of 10 nm the amplification should be approximately constant. Instead of that, the observed change in intensity can be attributed to the EAM, where the absorption depends more on the wavelength. Regarding the effect of the order of EAM and SOA, the observations for the different loops were again inconsistent. The amplification was larger for other loops for optical input going first into the SOA. But this is again not unexpected since, as already mentioned, the order should mainly affect the noise level and not the peak power.

This can be seen when considering the signal-to-noise ratio, which is shown in Fig. 31 b). The plots show that the difference in the signal-to-noise ratio is around 6 dB, which corresponds to the insertion loss of the EAM when no voltage is applied. That can be explained by the fact that when the SOA is in second place in the optical path, only the

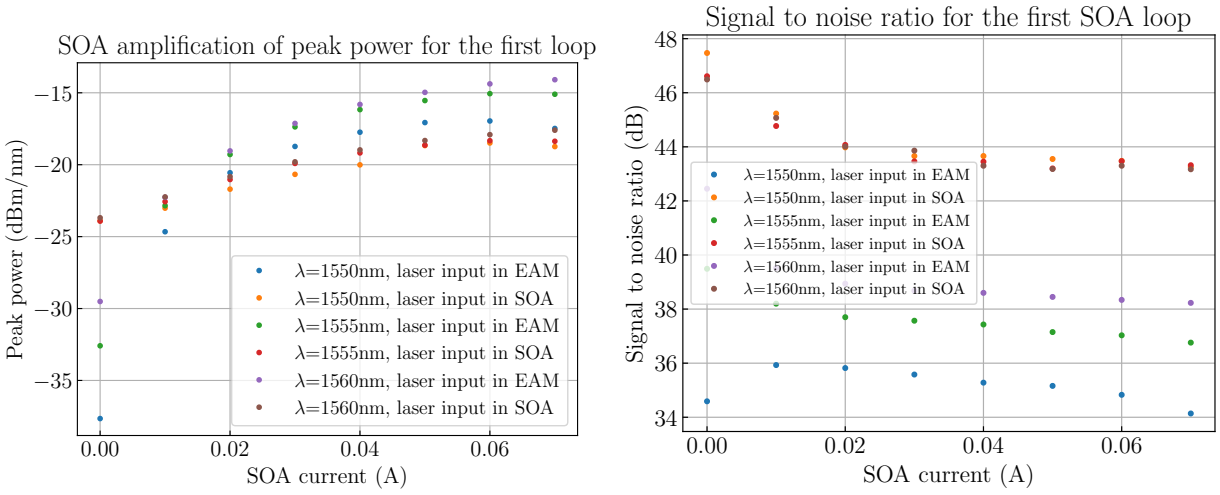

(a) (b)

Figure 31: Figure a) illustrates the amplification of peak power for the SOA on the first loop in relation to the SOA current. The sweep was conducted at three distinct wavelengths. Additionally, both orders were tested with the SOA first and then with the EAM first in the optical path. Figure b) shows the signal-to-noise ratio. This value is much higher when the optical power goes first into the SOA and second into the EAM.

signal experiences the EAM loss of -6 dB while no SOA noise gets absorbed. This behavior was consistent for all loops and for all sweeps.

To conclude, regarding the order of EAM and SOA, there is no significant effect on the modulation of the EAM or the amplification of the peak power, but the signal-to-noise ratio is much better when the SOA is the first device in the optical path.

However, on all structures on the chips, the EAM is always in the first place of the optical path. This is because the EAM is designed to modulate the laser signal rather than the noise of the SOA. Nevertheless, it seems that it might be more advantageous to position the SOA before the EAM in future chip designs.

Noise of the SOAs One of the most significant challenges was the high noise of some of the SOAs. The SOA of the left structure on the Laserchip had a noise power relative to the total power of -24 dB, which is more than two magnitudes, so a really small amount of noise. The ratio for the SOA loop test structure from the other chip was still 12 dB, which should still be suitable for modulation in order to encode information. But for the SOA on the four DFB structures on the Laserchip, the ratio of total power between noise and signal was only 1.2 dB. This is an insufficiently large ratio for a modulation that allows encoding information.

In order to determine the best approach for noise handling, the spectrum of the noise was inspected. Figure 32 illustrates the spectrum of the noise for the SOA of the left structure of the laser chip, as well as the SOA of the structure comprising four DFB lasers.

In both cases, the spectrum measurement was conducted using a single-mode fiber with optimized alignment, thus enabling a direct comparison of the actual absolute power. Figures 32 demonstrate that the noise level reaches a maximum at 1520 nm, after which it declines with increasing wavelength. This distribution is consistent with the expected

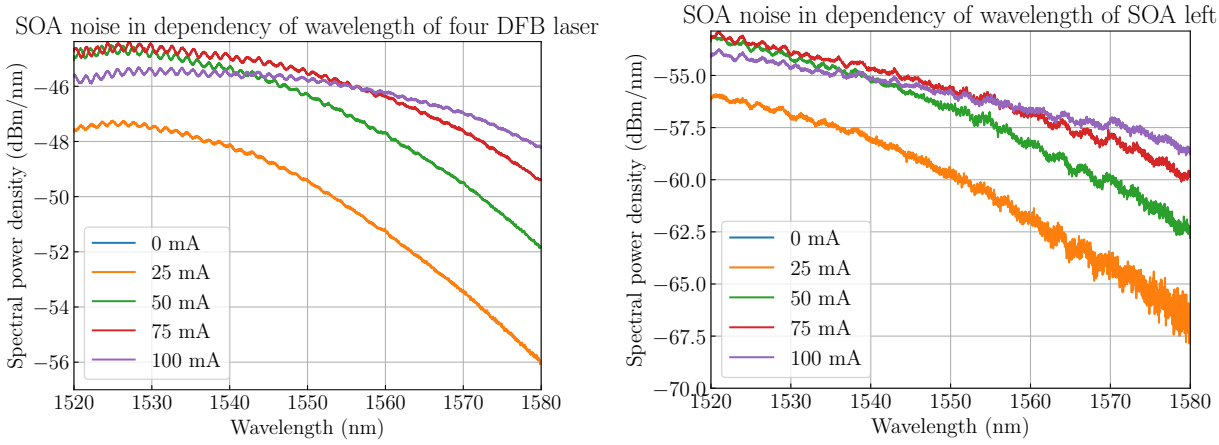

(a) (b)

Figure 32: The two figures illustrate the spectrum of SOA noise for the two SOAs on the laser chip. The curves in both figures exhibit a similar shape, with a reduction in noise intensity at higher wavelengths. However, the noise intensity in the left figure is considerably higher than in the right figure.

distribution. Nevertheless, as the ratio of the total powers indicated, the SOA noise production is quite different for theoretically identical SOAs.

Voltage-current-characteristic of the SOAs As with the DFB laser, the U-I curve is expected to correspond to a forward-biased diode-like profile which is shown in fig. 33

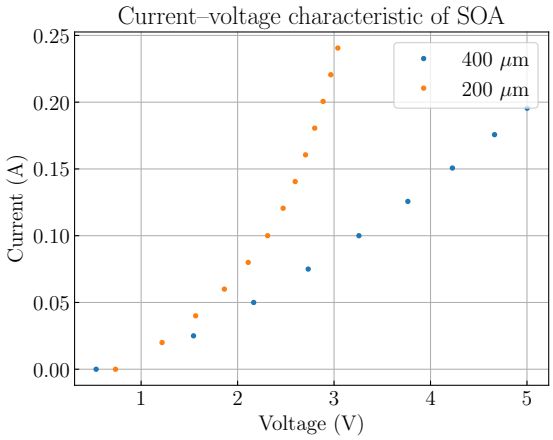

Figure 33: The figures illustrate the current-voltage characteristic of two distinct long SOAs. The SOA of the left graph is 400 µm long while the SOA of the left figure is 250 µm long.

In both figures, the plot follows the shape of a forward-biased diode. The difference is mainly the steeper slope of the shorter SOA. This can be attributed to the higher series resistor of the longer SOA.

Conclusions regarding SOAs It can be concluded that some of the SOAs are functioning as anticipated, like the long SOA with a gain of approximately 10 dB. Conversely, some of the shorter SOAs have a rather limited amplification, or even a net absorption, like the SOA in the structure of the four DFB lasers on the Laserchip. As previously stated, the generation of heat in the SOAs may potentially impair their functionality. One potential solution to this issue is to cool the InP chip. However, some other short SOAs worked as expected. So the problem is not that the short SOAs are in general not working but that they are unreliable in their functionality. Nevertheless, the loss of approximately -2 dB for an active-passive transition indicates that the use of these short SOAs is definitely rather disadvantageous than beneficial, particularly when the SOA is connected to both sides to waveguides instead of to other active components so that two butt-joints are necessary.

4.2.5 Photodiodes

Prior to testing the functionality of the photo diodes AC-coupled with a bias voltage, it was essential to assess their performance in DC mode. Therefore, the capacitance was short-circuited for grounding the cathodes. Given the low levels of the photocurrent, it is beneficial to use a transimpedance amplifier (TIA). A TIA converts the current into a proportional voltage, which can be measured by a regular voltmeter. The SOA current was set to 50 mA. An external laser was used to introduce varying laser intensities between 1 and 5 mW into the diode input with a wavelength of 1560 nm. The power is proportional to the photo current and the current is proportional to the TIA voltage. Hence, it was anticipated that a linear relationship would be observed between TIA voltages and laser power. Figure 34 shows the relationship between the TIA voltage and the laser input for the photodiodes.

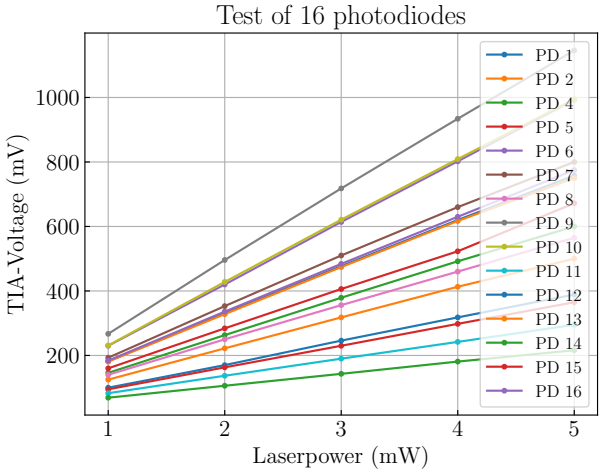

Figure 34: The figure illustrates the relationship between the TIA voltage and the laser input for the 16 photodiodes (besides PD3) with an SOA current of 50 mA. As expected, the relationship between the TIA voltage and the optical input power is linear.

The absolute TIA voltage value varies considerably between the different photo diodes. This discrepancy can be attributed to the fact that the alignment of the chip and the fiber array remained unchanged throughout the various measurements. Therefore, the alignment was not optimized for all photo diodes to the same extent. Nevertheless, all graphs show

approximately a linear relationship. The third photodiode (which is not shown) exhibited significantly lower voltages than the others. This can be explained by an incident where a forward-directed current of several milliamperes was applied to the photodiode for a longer time.

The linear relationship between power and TIA voltage was also examined for an unpumped SOA.

Additionally, for one photodiode, the SOA current was swept for a constant laser input. Figure 35 shows that the shape of the SOA current-TIA voltage curve is quite similar to the typical SOA current-power curve. This fulfils the expectations since power and TIA voltage should be proportional.

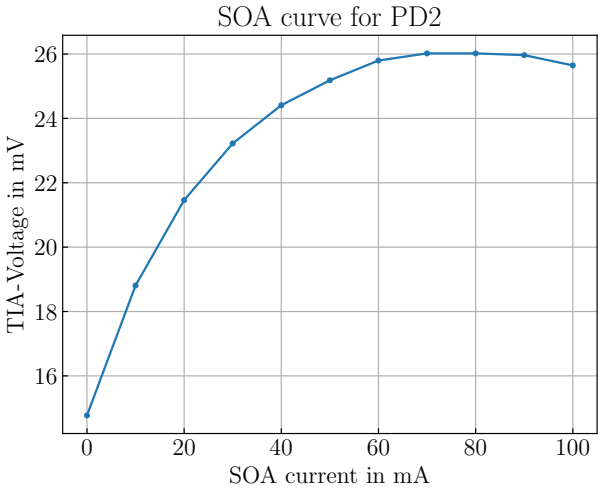

Figure 35: The figure illustrates the relationship between the TIA voltage and the SOA current, which follows the same shape of the peak power for a sweep of the other SOAs on the chips.

4.3 DC-operation with all building blocks

Up until this point, all components have been tested in single operation. So now the objective is to operate devices on the structure with the four DFB lasers on the Laserchip simultaneously.

4.3.1 Spectrum of four DFB-laser

In an initial experiment the spectrum will be examined when all four lasers are simultaneously operational at a current of 70 mA and the second DFB-heater gets swept.

As illustrated in fig. 36 for zero heat current, the peaks in the spectrum are relatively uniformly spaced, with a spacing of approximately 1.5 nm. By tuning the second DFB laser, it is possible to reach the neighboring peak for a tuning current of approximately 1.6 V. Nevertheless, the other DFB lasers are also affected in their wavelength due to the heat, resulting in a deviation of approximately 0.4 nm for neighboring lasers. It can be seen that it is possible to tune the laser, but it is important to note that the other wavelengths are also shifted.

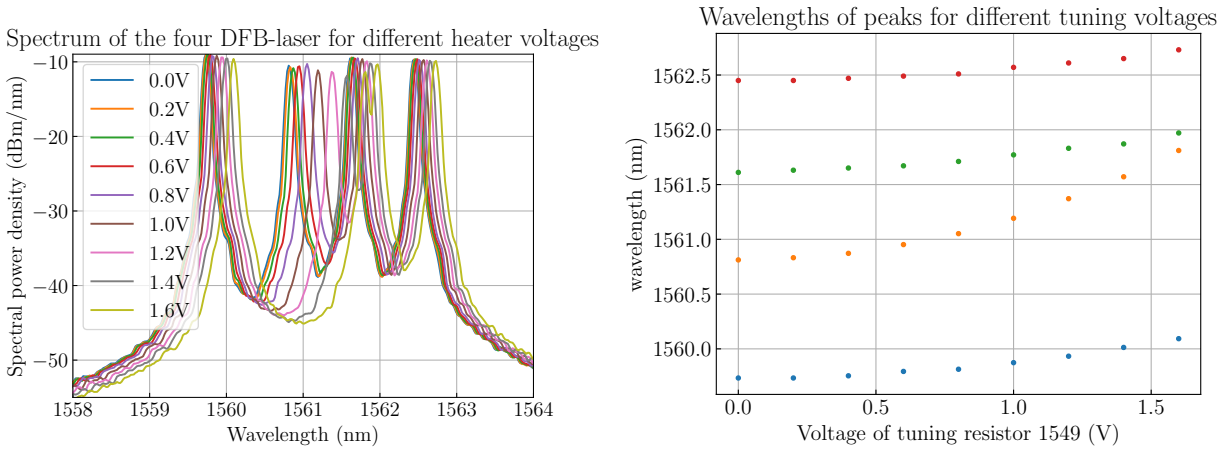

(a) (b)

Figure 36: The figure on the left illustrates the spectra of the multiplexed signal of the four DFB lasers for varying tuner voltages applied to the heater of the second laser. The right figure illustrates the wavelength position of the peaks. For a tuning voltage of 1.6V, the peaks for the second and the third lasers are almost merged into a single peak.

Equidistant spacing and special configuration of wavelengths The objective was to conduct two distinct tests using the lasers. The initial goal was to identify a wavelength configuration with a spacing as large as possible and as equidistant as possible. Therefore, the fourth laser with the highest wavelength was tuned with a 1 V tuning voltage to achieve a considerable degree of spacing, and subsequently, the middle two lasers were tuned in a manner that ensured equidistant spacing. Figure 37 a) illustrates the outcome of a spacing of approximately 2 nm.

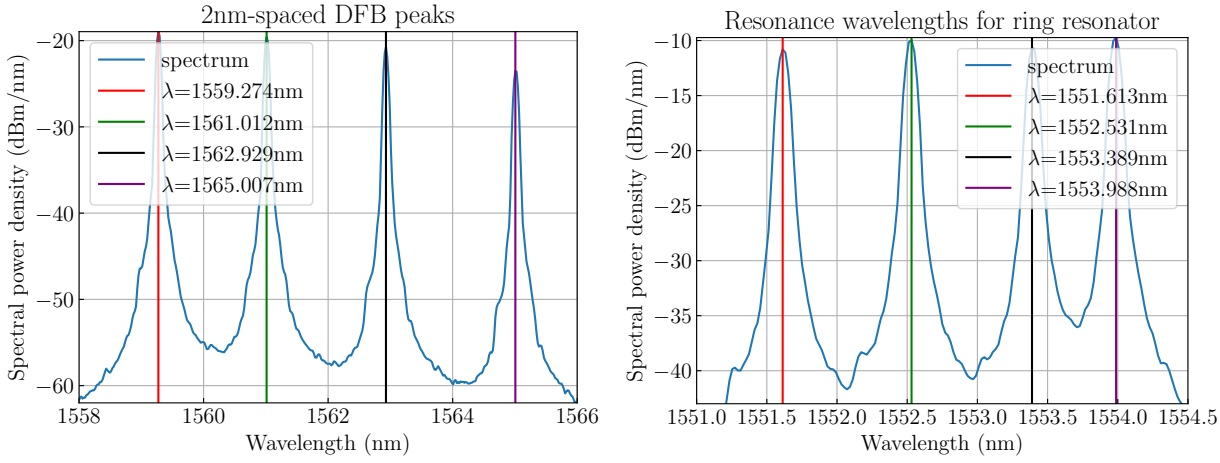

(a) (b)

Figure 37: The left figure illustrates the nearly 2 nm equidistant peak power spectrum for the four DFB lasers in a configuration where the tuner for the second laser is set to 1.4 V and the tuning voltage for the fourth laser is 1 V. The right figure illustrates a spectrum of the four DFB lasers, where the heaters have been tuned in order to achieve a specific configuration of peak wavelengths for a ring resonator.

In the next experiment, the objective was to achieve a specific configuration of wavelengths. The desired wavelengths were 1551.62 nm, 1552.55 nm, 1553.53 nm, and 1554.07 nm. Figure 37 b) shows the result that the requested wavelength configuration was successfully achieved with a deviation of 0.02 nm at maximum. The heater configuration was for the first laser a tuning voltage of 200 mV and for the third laser 300 mV. It can be noted that this time the aimed spacing was smaller than the spacing without any tuning. In that case, it is necessary to tune the first and second lasers with the smaller wavelengths since tuning can only increase the wavelength. For increasing the spacing, the third and fourth lasers must be tuned.

This specific wavelength configuration demonstrated in Figure 37 b) was essential for a combination of ring resonators used in another experiment conducted within the research group. Ring resonators consist of four connections. If a signal with a resonance wavelength propagates into the "input" connector, it will be transmitted to the "drop" connector. If the wavelength is not a resonance wavelength, the signal propagates to the "through" connector.

The requested wavelengths were the resonance wavelengths for ring resonators. So it was tested how much of the input signal reaches the "through" connector. The intensity that reached this connector was only 2 mW of the input power of 8 mW. Hence, this is an indicator that the requested wavelength configuration was achieved and most of the input power reached the "drop" connector of the ring resonator.

In conclusion, it is possible to hit specific wavelengths with precision. However, this is constrained by the necessity of a specific configuration of tuning voltages for each wavelength combination. This is due to the fact that any change in current on the chip affects the temperature of the entire chip.

Modulation and amplification of four wavelengths at the same time Furthermore, the capability of the EAM and SOA to modulate or amplify four wavelengths simultaneously was evaluated.

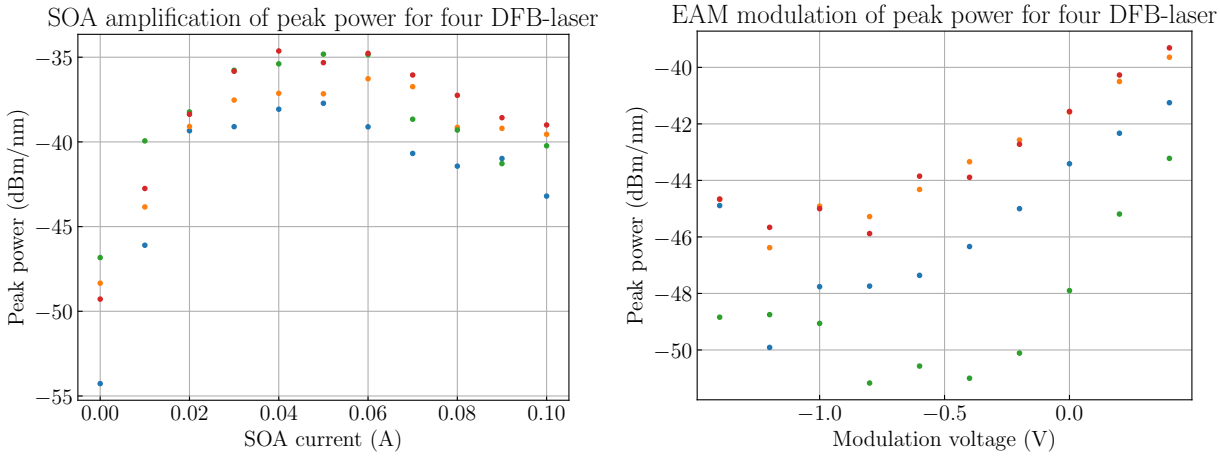

(a) (b)

Figure 38: The left figure illustrates the amplification of the peak power for varying SOA currents when all four DFB lasers are operating. The right figure illustrates the same phenomenon for the modulation of the EAM.

Figure 38 demonstrates that the SOA amplification and the EAM modulation for four DFB lasers simultaneously are similar to the amplification and modulation of a single wavelength. The discrepancy in peak intensity observed between different wavelengths is largely attributable to the differing peak intensities of the lasers, given that the DC-board exhibited minor discrepancies in current.

4.4 Determination of the symbol length for convolutional acceleration

Up to this point, all tests have been conducted in DC operation. Therefore, it is necessary to characterize the components for AC operation.

4.5 High frequency analysis

It is necessary to determine the frequency bandwidth of the modulators and the relevance of optimizing the electric conduction for high frequencies or terminating the devices with a 50 Ω parallel resistor.

Therefore, the detectorchip consists of a structure with four loops, including an SOA and an EAM. For the EAM in the first and fourth Loops, the conduction on the PCB is optimized. The third and fourth Loops are terminated by a resistor, whereas the first and second loops lack a resistor. Consequently, all possible combinations of termination and optimization are available.

4.5.1 Measuring the S_{11}parameter and the impedance

Utilizing the network vector analyzer (NVA), the S_{11} parameter is measured for all four EAMs. The power level of 0 dBm is applied, which corresponds to an amplitude of 0.32 V, assuming a 50 Ω impedance. The results for the S_{11}-parameter and the impedance as a function of frequency are presented in fig. 39.

As illustrated in fig. 39 a), the S_{11}-parameter exhibits an upward trajectory until reaching a maximum around 3 GHz, after which it declines. Furthermore, it can be observed that the parameter and the impedance undergo periodic increases and decreases, particularly in the case of non-terminated modulators. In general, there is no significant difference between the first and second Loops, which are both approximately 10 dB higher than the graphs for the third and fourth Loops. The fourth Loop is approximately 3 dB lower than the third. The impedance curve indicates that the oscillation for all modulators is approximately around 50 Ω, with the third Loop exhibiting a lower value of approximately 33 Ω. However, this result is against expectations since the main difference of the conduction for the third Loop was a narrower conductor on the PCB which is expected to have a higher impedance.

From the analysis of the S_{11}-parameter and the impedance plot, it can be concluded that the termination is especially important for high-frequency operation. However, optimized conduction seems to be crucial for achieving an optimal impedance of 50 Ω.

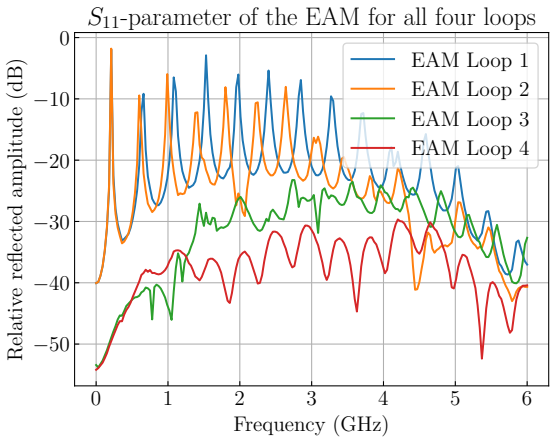

(a)

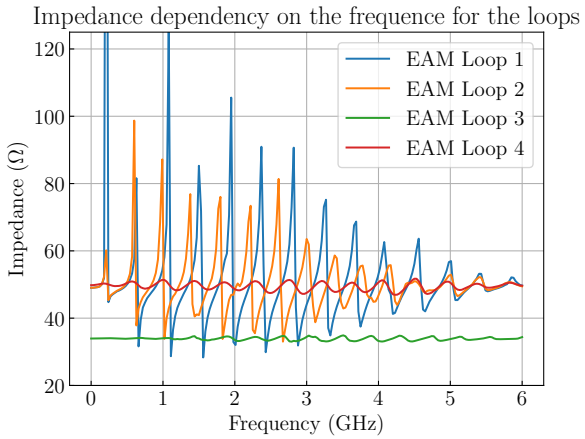

(b)

Figure 39: Figure a) shows the S_{11}-parameter for the EAM of the four loops, while fig. b) shows the impedance, estimated on the basis of the S_{11}-parameter. The EAMs of Loop one and two are without termination, while those from Loop three and four are terminated with a 50 Ω parallel resistor. Conduction in Loops one and four is optimized in contrast to Loops two and three.

4.5.2 Measuring the S_{21}parameter

In order to measure the S_{21}-parameter, it is necessary to connect one port of the VNA to the EAM as input and the other port to the photodiode as output. In this instance, the port connected to the EAM is equipped with a bias tee. A bias tee is a device that allows for the combination of a DC signal and an AC signal, resulting in an AC signal with a DC offset. The Keithley was used as the DC offset, with a working point of -0.6V selected. At this point, the EAM modulation is most linear. For the AC signal, a value of 0.32 V (0 dBm) is employed. The setup also consists of the external laser source as the input for the loops. The external photo diode measures the output intensity. The AC output of the photodiode is then connected to the other port of the VNA. Given that that absolute values cannot be determined for the S_{21}-parameter, the maximum value of the S_{21}-parameter plot was set to 0 dB. This allowed for the investigation of the S_{21}-parameter's

frequency-dependent behavior and its relative decline. Figure 40 illustrates the frequency at which the drop corresponds to -3 dB for all loops.

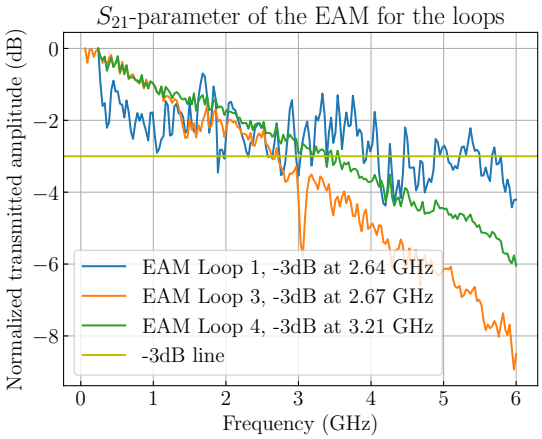

Figure 40: The figure depicts the S_{21}-parameter for the loops. The plot has been modified in such a way that the maximum transmission has been set to 0 dB. Additionally, the frequency at which the amplitude reached -3 dB of the maximum amplitude is shown.

A linear decline can be observed in the terminated EAMs, while the first EAM exhibits an irregular shape for the parameter dependent on frequency.

This linear decline for EAMs that are terminated with 50 Ω resistors was a similar result in literature for InP-based chips of the Heinrich-Hertz institute [16].

The decline in the third Loop is stronger than the one observed in the fourth Loop. It can thus be concluded from this graph that optimizing conduction is indeed beneficial.

It was tested whether it makes a difference for the S_{21}-parameter if the optical power goes first into the SOA or first into the EAM but there was no change observed.

Consequently, the determination of the S-parameters allows us to conclude that termination and optimization of the conduction are beneficial for devices that are intended to operate at high frequency. So the method used to optimize the conduction on the PCB is effective, or at the very least, more effective than the non-optimized conductions.

4.6 Determination of the symbol length for convolutional acceleration

As a last experimental part it shall be tried to make the necessary preparations for convolutional acceleration with the concept of time-wavelength interleaving. Therefore, the symbol length of the EAM on the four DFB structures must be determined

4.6.1 High frequency analysis of EAM of the four DFB lasers

First, it was interesting to see if the EAM in that structure was optimized for high frequency. So the same analysis that was carried out for the loops is done for that EAM. The results are shown in fig. 41.

It can be observed in the three figures that the results are indeed comparable to those obtained for the EAM on the fourth loop with optimized conduction and termination. So

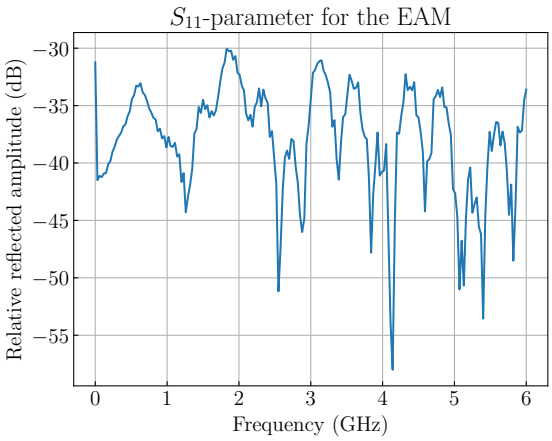

(a)

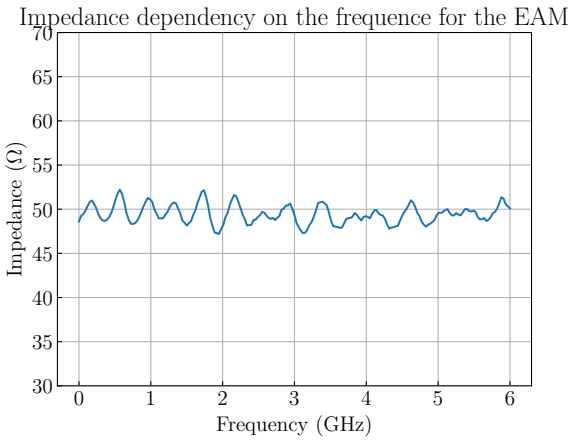

(b)

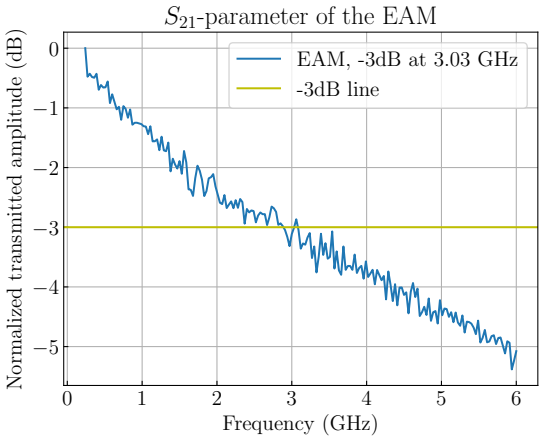

(c)

Figure 41: The three figures illustrate the high-frequency analysis of the EAM for the four DFB lasers. In the graphs, there is the S_{11}-parameter, the impedance, and the S_{21}-parameter shown in the dependency of the frequency. The outcomes are comparable to those observed for the EAM of the fourth loop, as anticipated, given that this EAM is also terminated and exhibits optimized conduction: The S_{11}-parameter is for all frequencies below -30dB, the calculated impedance is quite constant at 50 Ω for all frequencies and frequency of the -3 dB decline of the S_{21}-parameter is at around 3 GHz.

the EAM should be indeed optimized for the high frequency. However, it is first necessary to attempt to handle the noise generated by the SOA.

Noise handling with a filter Given the insufficient strength of the signal, it is necessary to implement external amplification in addition to the on-chip SOA. One of the limitations of the SOA on-chip is that it has a particularly poor signal-to-noise ratio. Figure 42 shows the peak power amplification and the signal-to-noise ratio for this SOA compared to the noise level.

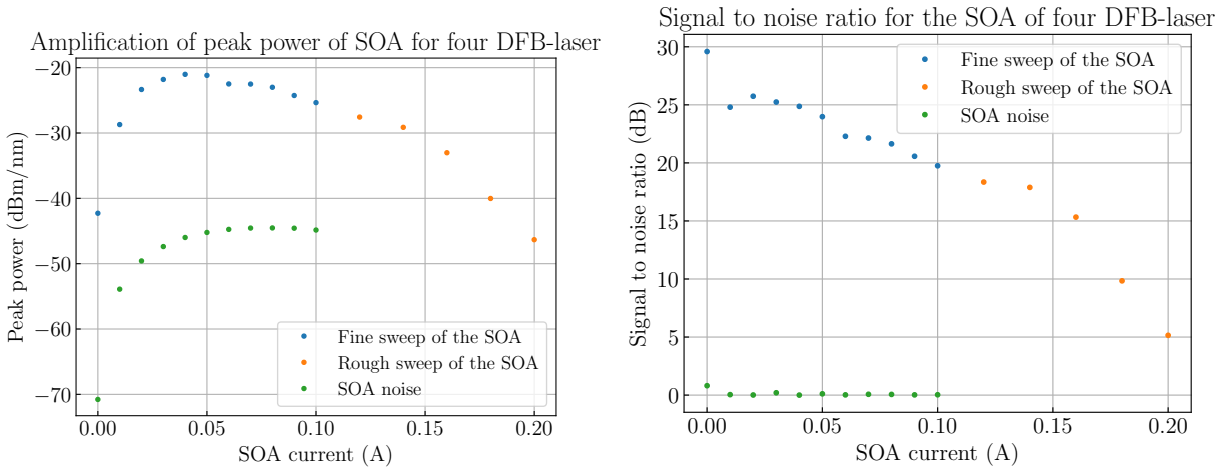

(a) (b)

Figure 42: The left figure illustrates the amplification of peak power for varying peak powers, alongside the noise level. The right figure illustrates the resulting signal-to-noise ratio. The signal-to-noise ratio is approximately 15 dB lower than that of the SOA from the test loop.

Since the signal has a relatively sharp spectrum while the noise is rather broad, it is attempted to enhance the signal-to-noise ratio and also the potential for modulation by utilizing a optical wavelength filter.

In order to ascertain the impact of the filter on the modulation of the total power, the spectral intensity must be integrated by adding all intensity values multiplied by the spacing of the measurement values. This value gives the total power.

Figure 43 shows that by using a filter, the modulation range of the total power could be increased from 1.5 dB to around 8 dB.

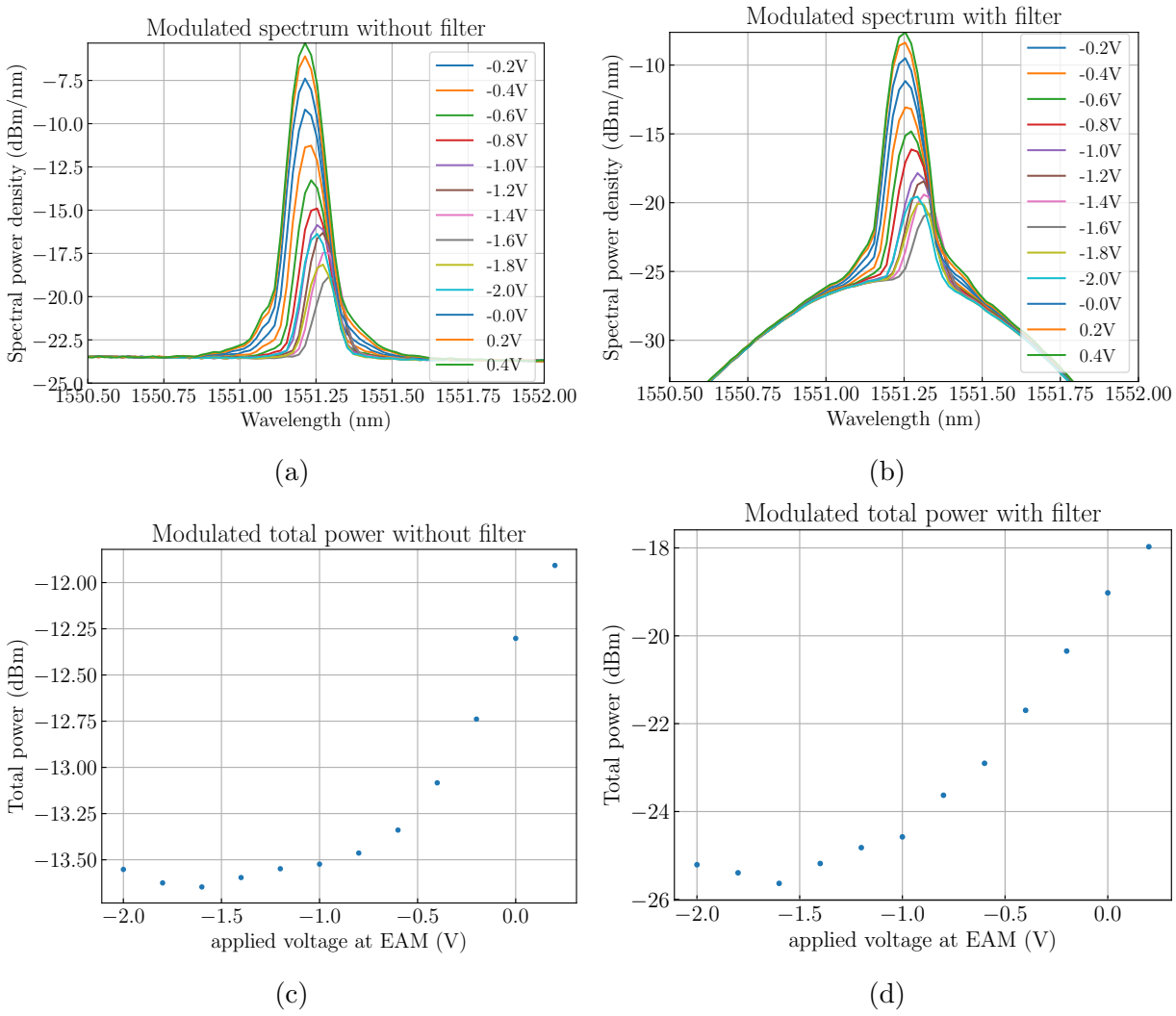

Figure 43: The two upper figures illustrate the spectra of the modulation of the EAM, with and without a filter, respectively. The lower figures illustrate the modulation of the resulting total power. The modulation with a filter is considerably greater than that without a filter.

Signal modulation with the EAM In order to determine the symbol length, the setup was identical to the one for estimating the S_{21}-parameter besides that the external photo diode was connected to an oscilloscope, and the AC input of the bias tee was connected to a frequency generator. The EAM was biased with a voltage of -0.1 volts. The first signal that was tried was a sinusoidal signal. The results for 1 GHz and 10 GHz can be observed in fig. 44.

However, it should be noted that the signal was averaged in order to achieve this presentation. Both screenshots were generated by triggering the function-generated curve. Without averaging, the signal appeared to be significantly distorted. When attempting to use another function than a sinusoidal function as modulation of the EAM, like a rectangular function or random data, it was not feasible to recognize the input data in the output of the photo diode.

Therefore, it was not possible to determine the symbol rate. The most probable expla-

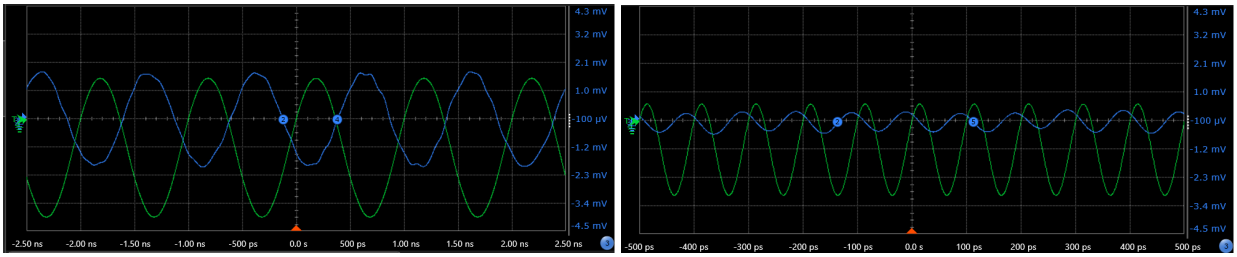

(a) Sinus signal for 1 GHz

(b) Sinus signal for 10 GHz

Figure 44: The images illustrate two oscilloscope screenshots. The green sinusoidal signal is generated by the frequency generator, while the blue curve represents the laser signal modulated by the EAM. The left image is for a frequency of 1 GHz, while the right image is for a frequency of 10 GHz. The EAM signal is averaged over a number of samples.

nation for this failure is that the signal-to-noise ratio is insufficient to obtain any results. Hence, this experiment failed, and it would be necessary to try the same experiment for an equivalent structure without an SOA or with an SOA with a better signal-to-noise ratio.

5 Conclusions

5.1 Functionality of the active components and conclusions for the structures on-chip

In summary, the building blocks function as anticipated so that they are suitable for the use in further experiments: The DFB lasers exhibit a significant deviation from the designed wavelength, yet this deviation is consistent on a single chip. Furthermore, the DFB lasers can be tuned up to around 1 nm. The power output is in a range up to 1-3 mW. The EAMs demonstrated a modulation range of 10 dB, although it was different for different EAMs for which voltages the modulation was the strongest and for which voltages the power saturates. So the working point has to be found for every EAM individually. With regard to the SOA, it can be concluded that the 400 µm-long SOA functioned as anticipated with an amplification of ca. 10 dB. The shorter SOAs exhibited considerable unreliability. Some of the devices functioned as expected, while for others the signal-to-noise ratio was only 1.2 dB, which was insufficient to encode any information or even to determine a symbol length. The photo diodes demonstrated an expected performance in DC mode. However, their functionality in AC mode has yet to be tested.

Based on these results, it can be concluded that SOAs should be used when they are longer, or if not they should be left out of the structures. It is particularly inadvisable to utilize an isolated SOA without connection to another active building block, as this necessitates two active-passive transistions with an insertion loss of around -2 dB for each butt-joint. Hence, with the estimated amplification of around 3 - 5 dB of these short SOAs in that case, it could even result in a net loss. It is therefore recommended that, for a structure such as one of the 16 photodiodes, the SOAs are to be excluded from the optical path. For the structure used in the attempt to perform time-wavelength interleaving, it would also be advisable to exclude the SOA when an external amplifier is used. An even better solution would be to use a longer SOA, thereby eliminating the necessity for an external amplifier. In this case, it would also be advantageous to connect the the active regions directly, thus eliminating the need for two butt-joints.

For the application of time-wavelength-interleaving, it would have been beneficial to increase the spacing of the DFB lasers for this structure. In the context of wavelength division multiplexing, the length of the dispersive element is approximately inversely proportional to the spacing of the different wavelengths. Consequently, it would be easier to perform this process by increasing the wavelength spacing so that the dispersive element could be shorter.

With regard to the order of modulation and amplification, it can be concluded that the signal-to-noise ratio is superior when the SOA is on the optical path before the EAM, so that the noise of the amplification gets reduced by the insertion loss of the EAM and not just the signal. For the peak power, there was no significant difference between the orders. So it might be advantageous to switch the position of the EAM and SOA in the two structures of the Laserchip.

By utilizing the tuners of the DFB laser, it was also possible to hit a specific configuration of wavelengths when all four DFB lasers on the Laserchip were operating simultaneously. However, for every configuration, it is necessary to find a new balance of the different heaters since tuning one laser affects the other lasers significantly due to thermal

crosstalk.

With regard to high frequencies, it can be observed that the termination with an appropriate parallel resistor is of even greater importance than the optimization of conduction. However, in order to achieve the most favorable results, it is recommended that both approaches are used.

Another general conclusion of the experiments is that it is advantageous to also include very simple test structures that allow for the assessment to the functionality of the devices individually. This means, for example, a structure like the one used to test the properties of the 400 µm-long SOA with one input and two outputs. One output should include a test device, and the other output should be without any modification as a reference path. This structure would have been quite suitable to test the properties of the short SOAs and the EAMs.

5.2 Summary and outlook

In this thesis, we were able to test all active components on the InP-chips in DC mode in single operation and, in the case of the four DFB structures, several components operating simultaneously. Furthermore, we conducted an analysis at high frequencies for the EAMs. The noise generated by the SOA proved to be a significant obstacle, preventing us from determining the symbol length. That would have been crucial to implementing the convolutional acceleration by time-wavelength interleaving. Unfortunately, even for a second chip of the same design, the relevant SOA showed this small signal-to-noise ratio again. So one option would be to design a new PCB for the Detectorchip since there is one structure that has not been considered yet, which consists of four DFB-lasers with an EAM and SOA. There, both active components are directly connected to each other so that there is not the extra loss of two butt-joints. Another option would be to design a new chip where this structure is realized without an SOA on-chip and using only off-chip amplifiers, or alternatively, with such a long SOA that no external amplifier is necessary.

Another subsequent step would be to examine the structure of the 16 photo diodes in AC operation and test whether the AC-coupling functions as intended. It would also be of interest to bond the structure of the 16 lasers on one of the laser chips, thus enabling both chips to be used for further experiments in a hybrid structure, which was their main purpose. For example, it might be interesting to connect them to a crossbar array structure on a silicon chip.

So as a final summary to assess the suitability of the InP-chips, it can be said that they appear quite suitable as laser sources and modulators for neuromorphic computing applications in our research group since the EAMs and the DFB-lasers worked as expected. When approaching close enough, in coupling and out oupling worked with a loss of -5.5 dB or even only -3 dB for a single-mode fiber. From the current perspective, the InP-chips seem suitable as detectors, but the photodiodes have so far only been tested for DC operation. However, in DC, they worked fully as expected. Also, the problems with the SOAs seem to be solvable when utilizing longer SOAs, so there is definitely a potential for specific neuromorphic applications with those chips like the approach of time-wavelength interleaving, although it was not possible to implement that for this thesis.

6 Appendix

6.1 Experimental devices

Voltage- and current source The Keithley 2400 SourceMeter is utilized as an electric source (current and voltage source) for the active components.

Free-space powermeter A free-space power meter is capable of measuring the optical output in a free-space environment. In this setup, the Thorlabs PM100D Optical Power and Energy Meter is used.

Fiber-coupled Powermeter In contrast to the free-space power meter, a fiber-coupled power meter is employed to measure the fiber-coupled optical power. The Thorlabs PM101R power meter is utilized for this purpose.

External laser source In order to implement an optical source for the loop structure on the chips, it is necessary to have an external laser source. In this instance, the Laser Santec TSL-770 is employed. The device is capable of wide-ranging wavelength tuning, spanning from 1480 to 1640 nm, and is capable of delivering an output power of up to 20 mW.

External amplifier In the event that the off-chip coupled signal is too small, it is possible to incorporate an external optical amplifier into the optical path with the objective of amplifying the signal. For this purpose, the PriTel LNHPFA-33 optical fiber amplifier is used.

Tunable optical filter It is a disadvantage of amplifiers, both external and on-chip SOAs, that they produce broad noise. To address this issue, a tunable optical filter can be employed to filter out all unwanted wavelengths. Therefore, the PriTel Tunable Filter Assembly TFA-1550 is used, which functions within the 1550 nm wavelength range and filters all wavelengths, with the exception of a 6 nm wide region within the wavelength spectrum.

Optical Spectrum Analyzer (OSA) The optical spectrum analyzer (OSA) used for this thesis is the Ando Optical Spectrum Analyzer AQ6330. The OSA displays the spectral wavelength density in power per nanometer. In order to obtain the total power, it is possible to integrate (or, in the case of the OSA with discrete bins, to sum) over the spectrum. The spectral resolution of the OSA must be higher than the one of the examined light sources which was for this model the case comparing tho the DFB-laser sources on the InP-chips.

External photodiode For this thesis, the Thorlabs RXM10AF is employed. This diode is designed to operate within the relevant wavelength range of 850–1550 nm, with an optical input, a display for the photocurrent, and one electronic DC output as well as an RF output, including a transimpedance amplifier (TIA).

Vector Network Analyzer (VNA) A network analyzer is employed to ascertain the characteristics of an electrical network. Therefore, the Rohde & Schwarz ZVL Vector Network Analyzer was used. This network vector analyzer (NVA) is equipped with two ports, enabling the measurement of the S_{11}-parameter as well as the S_{21}-parameter. To determine the parameters, the VNA applies an AC voltage in one port and measures the reflected amplitude for the S_{11} parameter in the same port, or in the case of the S_{21} parameter, the incoming amplitude in the other port. Furthermore, the instrument is capable of determining the impedance. Both S-parameters and the impedance are determined for frequencies up to 6 GHz.

Oscilloscope The Keysight UXR0104B real-time oscilloscope is employed to illustrate high-frequency signals. The device has multiple ports, allowing for the simultaneous display of the modulation signal from the function generator and the signal from the photodiode.

Function generator The M8195A 65 GSa/s Arbitrary Waveform Generator is utilized for the generation of signals that modulate the EAM with the objective of encoding information on the optical signals. The function generator is capable of producing various types of signals, including sinusoidal, rectangular, and random waveforms.

DC-Board For the experiments that needed more than three electric sources, a DC-Board was used that could be controlled by a graphic interface unit on the computer. The board contains several voltage sources and several current sources.

References

[1] Vincenzo De Maio, Atakan Aral, and Ivona Brandic. "A Roadmap To Post-Moore Era for Distributed Systems". en. In: *Proceedings of the 2022 Workshop on Advanced tools, programming languages, and PLatforms for Implementing and Evaluating algorithms for Distributed systems*. Salerno Italy: ACM, July 2022, pp. 30–34. ISBN: 978-1-4503-9280-8. DOI: 10.1145/3524053.3542747. URL: https://dl.acm.org/doi/10.1145/3524053.3542747 (visited on 07/11/2024).

[2] Manar Abu Talib et al. "A systematic literature review on hardware implementation of artificial intelligence algorithms". en. In: *The Journal of Supercomputing* 77.2 (Feb. 2021), pp. 1897–1938. ISSN: 0920-8542, 1573-0484. DOI: 10.1007/s11227-020-03325-8. URL: https://link.springer.com/10.1007/s11227-020-03325-8 (visited on 07/11/2024).

[3] Dennis V Christensen et al. "2022 roadmap on neuromorphic computing and engineering". en. In: *Neuromorphic Computing and Engineering* 2.2 (June 2022), p. 022501. ISSN: 2634-4386. DOI: 10.1088/2634-4386/ac4a83. URL: https://iopscience.iop.org/article/10.1088/2634-4386/ac4a83 (visited on 07/11/2024).

[4] Yesheng Li and Kah-Wee Ang. "Hardware Implementation of Neuromorphic Computing Using Large-Scale Memristor Crossbar Arrays". en. In: *Advanced Intelligent Systems* 3.1 (Jan. 2021), p. 2000137. ISSN: 2640-4567, 2640-4567. DOI: 10.1002/aisy.202000137. URL: https://onlinelibrary.wiley.com/doi/10.1002/aisy.202000137 (visited on 07/11/2024).

[5] Julien Borghetti et al. "'Memristive' switches enable 'stateful' logic operations via material implication". en. In: *Nature* 464.7290 (Apr. 2010), pp. 873–876. ISSN: 0028-0836, 1476-4687. DOI: 10.1038/nature08940. URL: https://www.nature.com/articles/nature08940 (visited on 07/11/2024).

[6] Shuo Wang and Fred C Lee. "Analysis and Applications of Parasitic Capacitance Cancellation Techniques for EMI Suppression". en. In: *IEEE Transactions on Industrial Electronics* 57.9 (Sept. 2010), pp. 3109–3117. ISSN: 0278-0046. DOI: 10.1109/TIE.2009.2038333. URL: http://ieeexplore.ieee.org/document/5371820/ (visited on 07/11/2024).

[7] Svetlana Nikolaevna Khonina et al. "Optical multiplexing techniques and their marriage for on-chip and optical fiber communication: a review". en. In: *Opto-Electronic Advances* 5.8 (2022), pp. 210127–210127. ISSN: 2096-4579. DOI: 10.29026/oea.2022.210127. URL: http://www.oejournal.org//article/doi/10.29026/oea.2022.210127 (visited on 07/11/2024).

[8] David A. B. Miller. "Attojoule Optoelectronics for Low-Energy Information Processing and Communications". en. In: *Journal of Lightwave Technology* 35.3 (Feb. 2017), pp. 346–396. ISSN: 0733-8724, 1558-2213. DOI: 10.1109/JLT.2017.2647779. URL: http://ieeexplore.ieee.org/document/7805240/ (visited on 07/11/2024).

[9] J. Feldmann et al. "Parallel convolutional processing using an integrated photonic tensor core". en. In: *Nature* 589.7840 (Jan. 2021). Number: 7840, pp. 52–58. ISSN: 0028-0836, 1476-4687. DOI: 10.1038/s41586-020-03070-1. URL: https://www.nature.com/articles/s41586-020-03070-1 (visited on 07/07/2024).

[10] Wim Bogaerts et al. “Programmable photonic circuits”. en. In: *Nature* 586.7828 (Oct. 2020), pp. 207–216. ISSN: 0028-0836, 1476-4687. DOI: 10.1038/s41586-020-2764-0. URL: https://www.nature.com/articles/s41586-020-2764-0 (visited on 07/12/2024).

[11] Christopher R. Doerr. “Silicon photonic integration in telecommunications”. en. In: *Frontiers in Physics* 3 (Aug. 2015). ISSN: 2296-424X. DOI: 10.3389/fphy.2015.00037. URL: http://journal.frontiersin.org/Article/10.3389/fphy.2015.00037/abstract (visited on 07/11/2024).

[12] Kaustubh Vyas et al. “Group III-V semiconductors as promising nonlinear integrated photonic platforms”. en. In: *Advances in Physics: X* 7.1 (Dec. 2022). Number: 1, p. 2097020. ISSN: 2374-6149. DOI: 10.1080/23746149.2022.2097020. URL: https://www.tandfonline.com/doi/full/10.1080/23746149.2022.2097020 (visited on 07/07/2024).

[13] Muhammad Rodlin Billah et al. “Hybrid integration of silicon photonics circuits and InP lasers by photonic wire bonding”. en. In: *Optica* 5.7 (July 2018), p. 876. ISSN: 2334-2536. DOI: 10.1364/OPTICA.5.000876. URL: https://opg.optica.org/abstract.cfm?URI=optica-5-7-876 (visited on 07/13/2024).

[14] Xingyuan Xu et al. “11 TOPS photonic convolutional accelerator for optical neural networks”. en. In: *Nature* 589.7840 (Jan. 2021). Number: 7840, pp. 44–51. ISSN: 0028-0836, 1476-4687. DOI: 10.1038/s41586-020-03063-0. URL: https://www.nature.com/articles/s41586-020-03063-0 (visited on 07/07/2024).

[15] Rongqing Hui. *Introduction to fiber-optic communications*. en. London: Academic press, 2020. ISBN: 978-0-12-805345-4.

[16] Francisco Soares et al. “InP-Based Foundry PICs for Optical Interconnects”. en. In: *Applied Sciences* 9.8 (Apr. 2019), p. 1588. ISSN: 2076-3417. DOI: 10.3390/app9081588. URL: https://www.mdpi.com/2076-3417/9/8/1588 (visited on 07/18/2024).

[17] L.B. Soldano and E.C.M. Pennings. “Optical multi-mode interference devices based on self-imaging: principles and applications”. en. In: *Journal of Lightwave Technology* 13.4 (Apr. 1995), pp. 615–627. ISSN: 07338724. DOI: 10.1109/50.372474. URL: http://ieeexplore.ieee.org/document/372474/ (visited on 07/11/2024).

[18] Herbert Venghaus and Norbert Grote, eds. *Fibre Optic Communication: Key Devices*. en. Vol. 161. Springer Series in Optical Sciences. Cham: Springer International Publishing, 2017. ISBN: 978-3-319-42365-4 978-3-319-42367-8. DOI: 10.1007/978-3-319-42367-8. URL: https://link.springer.com/10.1007/978-3-319-42367-8 (visited on 07/11/2024).

[19] Marius Grundmann. *The Physics of Semiconductors: An Introduction Including Nanophysics and Applications*. en. Graduate Texts in Physics. Cham: Springer International Publishing, 2021. ISBN: 978-3-030-51568-3 978-3-030-51569-0. DOI: 10.1007/978-3-030-51569-0. URL: http://link.springer.com/10.1007/978-3-030-51569-0 (visited on 07/07/2024).

[20] *PHOTODIODE BASICS – Wavelength Electronics*. URL: https://www.teamwavelength.com/maintenance/photodiode-basics/ (visited on 07/11/2024).

[21] Keh Yung Cheng. *III–V Compound Semiconductors and Devices: An Introduction to Fundamentals*. en. Graduate Texts in Physics. Cham: Springer International Publishing, 2020. ISBN: 978-3-030-51901-8 978-3-030-51903-2. DOI: 10.1007/978-3-030-51903-2. URL: http://link.springer.com/10.1007/978-3-030-51903-2 (visited on 07/11/2024).

[22] Ekbert Hering, Julian Endres, and Jürgen Gutekunst, eds. *Elektronik für Ingenieure und Naturwissenschaftler*. de. Berlin, Heidelberg: Springer Berlin Heidelberg, 2021. ISBN: 978-3-662-62697-9 978-3-662-62698-6. DOI: 10.1007/978-3-662-62698-6. URL: https://link.springer.com/10.1007/978-3-662-62698-6 (visited on 07/07/2024).

[23] Frank Brückerhoff-Plückelmann et al. "Chalcogenide phase-change devices for neuromorphic photonic computing". en. In: *Journal of Applied Physics* 129.15 (Apr. 2021). Number: 15, p. 151103. ISSN: 0021-8979, 1089-7550. DOI: 10.1063/5.0042549. URL: https://pubs.aip.org/jap/article/129/15/151103/1056474/Chalcogenide-phase-change-devices-for-neuromorphic (visited on 07/07/2024).

7 Acknowledgements

First of all, I would like to thank my supervisor Lennart, for all the guidance and support to complete my projects, for introducing me to scientific workin, for giving me much freedom in what I was doing and always being ready to help me, and of course for revising even quite early stages of this thesis. In particular, I would like to thank him for creating an atmosphere where it was really fun to do my project.

I would also like to thank Julius for introducing me to KICad, helping me with all electronic and setup-related problems, and also proofreading my thesis.

Furthermore, I would like to thank Ralf for always being ready and quick to wire-bond six different chips during the time I was in the research group.

I would like to thank Erik, Jelle, and Falk for always helping out spontaneously from time to time.

I would also like to thank Julia and Sophia for revising my thesis regarding language errors.

And of course, thanks to Prof. Pernice for giving me the opportunity to do my bachelor thesis in his group, and also to Prof. Schmidt for agreeing to be my second corrector.

For transparency, I used the AI tool DeepL for translation, rephrasing, and grammar correction.

8 Erklärung / Declaration

Ich versichere, dass ich diese Arbeit selbstständig verfasst und keine anderen als die angegebenen Quellen und Hilfsmittel benutzt habe.

I certify that I have written this thesis independently and have not used any sources or aids other than those specified.

Heidelberg, 21.07.2024